Journal of Computational Physics 305 (2016) 185–207

Contents lists available at ScienceDirect

Journal of Computational Physics

www.elsevier.com/locate/jcp

Dynamic earthquake rupture simulations on nonplanar faults embedded in 3D geometrically complex, heterogeneous elastic solids

Kenneth Duru [a,*], Eric M. Dunham [a,b]

[a] Department of Geophysics, Stanford University, Stanford, CA, United States
[b] Institute for Computational and Mathematical Engineering, Stanford University, Stanford, CA, United States

ARTICLE INFO

Article history:
Received 15 December 2014
Received in revised form 12 October 2015
Accepted 13 October 2015
Available online 19 October 2015

Keywords:
Earthquake rupture dynamics
Elastic waves
Nonlinear friction laws
Interface conditions
Interface waves
Curvilinear grids
Coordinate transformation
High order accuracy
Time-stability
Summation-by-parts finite difference method
Penalty method

ABSTRACT

Dynamic propagation of shear ruptures on a frictional interface in an elastic solid is a useful idealization of natural earthquakes. The conditions relating discontinuities in particle velocities across fault zones and tractions acting on the fault are often expressed as nonlinear friction laws. The corresponding initial boundary value problems are both numerically and computationally challenging. In addition, seismic waves generated by earthquake ruptures must be propagated for many wavelengths away from the fault. Therefore, reliable and efficient numerical simulations require both provably stable and high order accurate numerical methods.

We present a high order accurate finite difference method for: a) enforcing nonlinear friction laws, in a consistent and provably stable manner, suitable for efficient explicit time integration; b) dynamic propagation of earthquake ruptures along nonplanar faults; and c) accurate propagation of seismic waves in heterogeneous media with free surface topography.

We solve the first order form of the 3D elastic wave equation on a boundary-conforming curvilinear mesh, in terms of particle velocities and stresses that are collocated in space and time, using summation-by-parts (SBP) finite difference operators in space. Boundary and interface conditions are imposed weakly using penalties. By deriving semi-discrete energy estimates analogous to the continuous energy estimates we prove numerical stability. The finite difference stencils used in this paper are sixth order accurate in the interior and third order accurate close to the boundaries. However, the method is applicable to any spatial operator with a diagonal norm satisfying the SBP property. Time stepping is performed with a 4th order accurate explicit low storage Runge–Kutta scheme, thus yielding a globally fourth order accurate method in both space and time. We show numerical simulations on band limited self-similar fractal faults revealing the complexity of rupture dynamics on rough faults.

* Corresponding author.
E-mail address: kduru@stanford.edu (K. Duru).

http://dx.doi.org/10.1016/j.jcp.2015.10.021
0021-9991/

1. Introduction

Spontaneously propagating shear ruptures along frictional interfaces embedded in elastic solids occur in many solid mechanics and geophysical problems [51,21,49,31,44,2,41,46,48,45,47,55,4,3]. For example during an earthquake, two sides of the fault, initially held in contact by a high level of frictional resistance, slip suddenly when that resistance catastrophically decreases, generating strong ground shaking which is carried by seismic (elastic) waves to remote areas, far away from fault zones. Thus efficient and reliable simulations of earthquake ruptures and the resulting strong ground motion form a crucial component of earthquake-hazard analysis. The discontinuity in the tangential displacements across a fault zone is referred to as slip. Seismic waves generated by slip on one part of the fault transmit stresses to adjacent parts of the fault, possibly causing that part of the fault to slip and leading to the progressive propagation of ruptures. A typical dynamic earthquake rupture model couples the equations of linear elastodynamics to friction laws at the fault. The friction laws are generally expressed as nonlinear relations between tractions acting on the fault and the slip rate. The catastrophic initiation of slip and the sliding motion of the fault across the interface are captured via the interaction of friction and elastic waves. In dynamic earthquake rupture models, the earthquake source process is not known a priori, but is determined as part of the solution. The corresponding initial boundary value problem (IBVP) can be ill-conditioned, and poses several numerical and computational challenges. In addition, seismic waves generated by earthquake ruptures must be propagated many wavelengths far away from the fault. Therefore, reliable and efficient numerical simulations require both provably stable and high order accurate numerical methods.

A number of numerical methods have been developed for computational modeling of earthquake rupture dynamics. Classical finite difference methods (on planar faults) have been widely used [12,5,35,38]. Some of these methods have been extended to nonplanar fault geometries using curvilinear grids and coordinate transformation techniques [32], or by aligning the fault surface through cell diagonals [10,11]. However, the presence of nonlinear boundary and interface conditions, and discontinuities in media parameters make the design of stable and accurate finite difference methods challenging. The method developed in [32] for two space dimensional (2D) models can be proven stable; others produce solutions that appear accurate before eventually diverging, or require artificial dissipation of some form to stabilize the method. Another historical and popular class of methods for earthquake rupture dynamics is boundary element methods [46,22,48,2]. Thus far, these methods have been limited to uniform elastic materials. They can also handle nonplanar faults, with the exception of the spectral boundary integral equation method [22]. It is particularly noteworthy that spectral boundary integral equation methods are effective for planar fault problems, and have been extensively used to study fault weakening processes.

Unstructured discretizations such as continuous Galerkin finite element methods [25,34,1,14,18] and discontinuous Galerkin (dG) finite element/volume methods [13,42,56] have also been developed for earthquake rupture dynamics. The power of unstructured methods lies in their ability to resolve complex fault geometries. However, generation of a high quality unstructured mesh can be a non-trivial problem in itself. Unstructured discretizations also require extra bookkeeping and additional memory to keep track of the connectivity of the grid. Nonetheless, continuous Galerkin finite element methods are quite popular for rupture dynamics. In practice these methods have been limited to second order accuracy due to lumping of the mass matrix, which is necessary for computational efficiency. Since second order accuracy is not sufficient to propagate waves to remote areas, high order finite element methods have also been considered. Spectral element and dG finite element/volume methods [27,13,42,56] have been developed, yielding diagonal or locally block diagonal mass matrices. There are also potential drawbacks for these methods, due to doubling of the number of degrees of freedom along the element edges, and restrictive time-steps particularly for high order methods.

In this study, we develop a provably stable and high order accurate finite difference method for earthquake rupture dynamics on nonplanar faults embedded in three space dimensional (3D) geometrically complex, heterogeneous Earth models. In particular, we solve the first order form of the 3D elastic wave equation on a boundary-conforming curvilinear mesh, subject to traction free boundary conditions at the Earth's surface and nonlinear friction laws at the fault. The unknown field variables are particle velocities and stress fields that are collocated in space and time. Prior to numerical approximations, we transform the equations and boundary/interface conditions to computational cubes where numerical approximations of spatial derivatives can be performed efficiently. However, the coordinate transformation must be carefully introduced such that the transformed system of partial differential equations (PDEs) is numerically tractable. For linear hyperbolic problems in multiple dimensions, the SBP property is not sufficient for numerical stability [30,32]. This is because the way the metric terms enter the transformed system of PDEs and product rule does not explicitly hold for finite difference operators. This is truly a fundamental problem for numerical approximation of spatial derivatives on curvilinear meshes/elements [40,29,28,30,57,39,54,26,32]. Previous work has suggested to split the transformed equations into conservative and non-conservative parts such that the transformed equation is skew-symmetric [29,30,39,32]. This is critical for numerical stability. Unfortunately, splitting the equations increases the expected number of floating point operations. This is undesirable, particularly because of the sheer size of the problem in 3D. In this paper, we propose a new way to transform the equations of linear elastodynamics, which reduces the expected number of floating points operations at least by half while ensuring numerical stability. We use two different representations of the spatial derivatives: nonconservative form for the velocity fields and conservative form for the stress fields. This enables the construction of a continuous energy estimate, for the transformed equations, which can be mimicked to develop stable numerical approximations. After we have performed the coordinate transformation to the computational domain, the transformed equations are then discretized in space using high order accurate summation-by-parts (SBP) finite difference operators [53,36,23].

Next, we turn our attention to the boundary and interface conditions. The interface conditions are nonlinear friction laws. If appropriate care is not taken the numerical treatment of the interface conditions can introduce artificial numerical stiffness, thus preventing the use of efficient explicit time-stepping schemes [19,32]. To succeed, we construct a subspace of solutions satisfying the (discrete) linear elastodynamics equations and the interface condition exactly. We then project the solutions on the interface to this subspace, extracting data. The boundary and interface conditions with appropriate data are enforced weakly using a penalty technique referred to as the simultaneous approximation term (SAT) method [9,36]. By deriving penalty parameters and constructing discrete energy estimates we prove asymptotic stability of the semi-discrete system. Time integration is performed using a fourth order accurate low storage Runge–Kutta scheme [8]. The SBP operators used in this study are sixth order accurate in the interior with third order accurate boundary closure, thus yielding globally a fourth order accurate scheme in both time and space. Since we have used the SBP–SAT methodology, our technique is in spirit similar to the method developed in [32] for 2D problems. However, the coordinate transforms, numerical approximation of the interior problem and the penalty parameters derived in this paper are different from [32] in general curvilinear grids. Moreover, while the method developed in [32] is limited to 2D isotropic elasticity our method is applicable to arbitrary linear elastic media in 3D.

We have performed numerical experiments verifying stability, high order accuracy, and demonstrating the potential of our method in simulating earthquake rupture dynamics on nonplanar faults embedded in 3D geometrically complex, heterogeneous Earth models. In particular, we have considered both slip-weakening and rate-and-state friction laws on nonplanar faults, including recent benchmark problems proposed by SCEC/USGS Dynamic Earthquake Rupture Code Verification Project (http://scecdata.usc.edu/cvws/). We also show simulations on fractal faults revealing the complexity of rupture dynamics on rough faults.

The remainder of the paper will proceed in the following manner. In the next section, we introduce the equations of linear elastodynamics in a general medium and 3D geometrically complex domain. Then we discuss wave modes, curvilinear coordinates and coordinate transformations as well as appropriate boundary conditions, and derive energy estimates. In Section 3, we present the friction laws governing the dynamics of the fault, and derive corresponding energy estimates. In Section 4, we discretize the equations with the boundary and interface conditions implemented using penalties. Numerical stability is proven using the energy method. In Section 5, we present numerical experiments verifying high order accuracy and demonstrating the potential of the method for earthquake rupture dynamics on rough faults embedded in 3D geometrically complex, heterogeneous Earth models. A summary of the paper and suggestions for future work are offered in the last section.

2. The elastic wave equation

Let t denote the time variable and the Cartesian coordinates of a three dimensional spatial domain defined by (x, y, z). Consider the first order form of the time-dependent elastic wave equation in a source free, heterogeneous medium,

$$\begin{pmatrix} \rho \frac{\partial v_x}{\partial t} \\ \rho \frac{\partial v_y}{\partial t} \\ \rho \frac{\partial v_z}{\partial t} \\ \mathbf{S}\begin{pmatrix} \frac{\partial \sigma_{xx}}{\partial t} \\ \frac{\partial \sigma_{yy}}{\partial t} \\ \frac{\partial \sigma_{zz}}{\partial t} \\ \frac{\partial \sigma_{xy}}{\partial t} \\ \frac{\partial \sigma_{xz}}{\partial t} \\ \frac{\partial \sigma_{yz}}{\partial t} \end{pmatrix} \end{pmatrix} = \begin{pmatrix} \frac{\partial \sigma_{xx}}{\partial x} + \frac{\partial \sigma_{xy}}{\partial y} + \frac{\partial \sigma_{xz}}{\partial z} \\ \frac{\partial \sigma_{xy}}{\partial x} + \frac{\partial \sigma_{yy}}{\partial y} + \frac{\partial \sigma_{yz}}{\partial z} \\ \frac{\partial \sigma_{xz}}{\partial x} + \frac{\partial \sigma_{yz}}{\partial y} + \frac{\partial \sigma_{zz}}{\partial z} \\ \frac{\partial v_x}{\partial x} \\ \frac{\partial v_y}{\partial y} \\ \frac{\partial v_z}{\partial z} \\ \frac{\partial v_x}{\partial y} + \frac{\partial v_y}{\partial x} \\ \frac{\partial v_x}{\partial z} + \frac{\partial v_z}{\partial x} \\ \frac{\partial v_y}{\partial z} + \frac{\partial v_z}{\partial y} \end{pmatrix}, \tag{1}$$

where $(v_x, v_y, v_z)^T$ are the particle velocities, and $(\sigma_{xx}, \sigma_{yy}, \sigma_{zz}, \sigma_{xy}, \sigma_{xz}, \sigma_{yz})^T$ are the stresses. At the initial time $t = t_0 \geq 0$, we set initial data for particle velocities and stresses. The elastic medium is described by the density $\rho(x, y, z)$ and the compliance matrix $\mathbf{S} = \mathbf{C}^{-1}$, where $\mathbf{C} = \mathbf{C}^T > 0$ is the stiffness matrix. Since the stiffness matrix is symmetric positive definite, it also follows that the compliance matrix is symmetric positive definite, $\mathbf{S} = \mathbf{S}^T > 0$. Note that the stiffness matrix depends on the spatial variables (x, y, z). In a general medium the stiffness matrix $\mathbf{C}$ is described by 21 independent elastic coefficients. In the isotropic case, the medium is described by two independent elastic coefficients, the Lamé parameters λ, μ, and

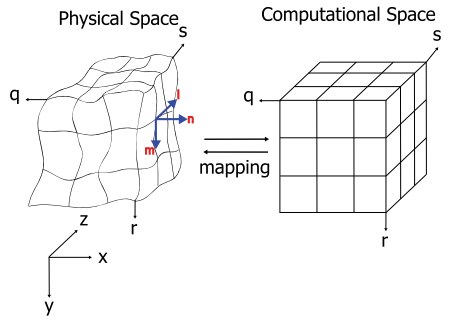

Fig. 1. Boundary conforming curvilinear grids and coordinate transformation.

$$\mathbf{C} = \begin{pmatrix} 2\mu+\lambda & \lambda & \lambda & 0 & 0 & 0 \\ \lambda & 2\mu+\lambda & \lambda & 0 & 0 & 0 \\ \lambda & \lambda & 2\mu+\lambda & 0 & 0 & 0 \\ 0 & 0 & 0 & \mu & 0 & 0 \\ 0 & 0 & 0 & 0 & \mu & 0 \\ 0 & 0 & 0 & 0 & 0 & \mu \end{pmatrix}.$$

2.1. Wave modes

In order to discuss wave modes it is convenient to rewrite the elastic wave equation (1) as a first order hyperbolic system

$$\frac{\partial \mathbf{U}}{\partial t} = A_x \frac{\partial \mathbf{U}}{\partial x} + A_y \frac{\partial \mathbf{U}}{\partial y} + A_z \frac{\partial \mathbf{U}}{\partial z}. \tag{2}$$

Here, $\mathbf{U} = \left(v_x, v_y, v_z, \sigma_{xx}, \sigma_{yy}, \sigma_{zz}, \sigma_{xy}, \sigma_{xz}, \sigma_{yz}\right)^T$ and the coefficient matrices A_x, A_y, A_z are determined by the density ρ and the stiffness matrix $\mathbf{C}$. To describe the wave properties of the medium, we consider constant coefficients and introduce the plane wave solution

$$\mathbf{U} = \mathbf{U}_0 e^{i\omega t + ik_x x + ik_y y + ik_z z}, \quad \text{with} \quad k_x^2 + k_y^2 + k_z^2 = 1, \quad i = \sqrt{-1}, \tag{3}$$

in (2). Thus we obtain

$$\omega \mathbf{U}_0 = \left(k_x A_x + k_y A_y + k_z A_z\right) \mathbf{U}_0.$$

Note that $\mathbf{k} = \left(k_x, k_y, k_z\right)$ is an arbitrary unit vector denoting the normalized propagation direction of the plane wave (3). The normalized angular frequency ω and the polarization vector $\mathbf{u}_0$ are the eigenvalues and eigenvectors, respectively, of the matrix

$$\boldsymbol{\Upsilon}\left(k_x, k_y, k_z\right) = k_x A_x + k_y A_y + k_z A_z. \tag{4}$$

It is well-known that the matrix $\boldsymbol{\Upsilon}\left(k_x, k_y, k_z\right)$ is symmetric (or can be symmetrized). The eigenvalues ω are real and the eigenvectors are complete. The matrix $\boldsymbol{\Upsilon}\left(k_x, k_y, k_z\right)$ has six non-zero eigenvalues $\omega_1 = c_n$, $\omega_2 = -c_n$, $\omega_3 = c_m$, $\omega_4 = -c_m$, $\omega_5 = c_l$, $\omega_6 = -c_l$, and three zero eigenvalues $\omega_7 = \omega_8 = \omega_9 = 0$. Note that we have arranged the eigenvalues and eigenvectors such that $c_n \geq c_m \geq c_l > 0$.

An eigen-pair ω_j, $\mathbf{u}_{0j}$ describes a wave mode and the wave speed is given by $|\omega_j|$. The eigen-pairs with $\omega_j = 0$ correspond to temporally constant wave modes. In the absence of boundaries, the elastic wave equation (1) supports one p-wave mode and two s-wave modes. The p-wave speed is given by c_n and s-wave speeds are c_m, c_l. For a general medium the two s-waves can have different wave-speeds. However, in an isotropic medium the s-waves have an identical wave-speed $c_m = c_l$.

2.2. Curvilinear coordinates and coordinate transformation

For geometrically complex models, numerical treatments can be simplified if there is a smooth coordinate transformation from the physical space to a reference computational cube (Fig. 1). Consider the elastic wave equation (1) in a domain with arbitrarily shaped smooth boundaries. Let one of the boundaries of the domain be located at $x = \widetilde{x}(y, z)$, where $\widetilde{x}(y, z)$ is a function describing the surface of the boundary. In principle, it is possible to construct a boundary conforming curvilinear mesh, with the coordinates (x, y, z), representing the domain. We introduce a smooth grid mapping [43] from the curvilinear mesh to the unit cube $(q, r, s) \in [0, 1] \times [0, 1] \times [0, 1]$ defined by:

$$\left(x(q,r,s), y(q,r,s), z(q,r,s)\right) \leftrightarrow \left(q(x,y,z), r(x,y,z), s(x,y,z)\right). \tag{5}$$

We have chosen coordinates such that the boundary $(\widetilde{x}(y,z),y,z)$ in the physical space is now located at $(q=1,r,s)$. The Jacobian and metric coefficients are defined by

$$J = x_q\left(y_r z_s - z_r y_s\right) - y_q\left(x_r z_s - z_r x_s\right) + z_q\left(x_r y_s - y_r x_s\right) > 0, \tag{6}$$

$$\begin{aligned} Jq_x &= \left(y_r z_s - z_r y_s\right), \quad Jr_x = \left(z_q y_s - y_q z_s\right), \quad Js_x = \left(y_q z_r - z_q y_r\right), \\ Jq_y &= \left(z_r x_s - x_r z_s\right), \quad Jr_y = \left(x_q z_s - z_q x_s\right), \quad Js_y = \left(z_q x_r - x_q z_r\right), \\ Jq_z &= \left(x_r y_s - y_r x_s\right), \quad Jr_z = \left(y_q x_s - y_s x_q\right), \quad Js_z = \left(x_q y_r - x_r y_q\right). \end{aligned} \tag{7}$$

Here, the subscripts denote partial derivatives, that is $q_x = \frac{\partial q}{\partial x}$, $x_q = \frac{\partial x}{\partial q}$, etc. It is possible to rewrite the metric terms in (7) such that the numerical approximation of the metric terms and their derivatives satisfy exactly the same metric identities as the continuous metric derivatives. For example the first row in (7) can be rewritten as [28,57]

$$\begin{aligned} \left(y_r z_s - z_r y_s\right) &= \frac{1}{2}\left(y_r z - z_r y\right)_s - \frac{1}{2}\left(z y_s - y z_s\right)_r, \quad \left(z_q y_s - y_q z_s\right) = \frac{1}{2}\left(z_q y - y_q z\right)_s - \frac{1}{2}\left(y z_s - z y_s\right)_q, \\ \left(y_q z_r - z_q y_r\right) &= \frac{1}{2}\left(y_q z - z_q y\right)_r - \frac{1}{2}\left(z y_r - y z_r\right)_q. \end{aligned} \tag{8}$$

The second and third rows of (7) can be rewritten in the same manner as in (8).

Remark 1. Note that we have assumed that the curvilinear mesh is sufficiently smooth such that the Jacobian and all metric coefficients can be computed efficiently from the mesh. Here, it is sufficient to assume that the Jacobian defined in (6) is positive and bounded, $0 < J < \infty$ everywhere in the computational space. More elaborate discussions on the impact of mesh quality on numerical simulations of partial differential equations can be found in [26], and in the references therein.

We will now transform the elastic wave equation from the physical space to the computational space. We will use two different transformations of the spatial derivatives in the transformed coordinates. Spatial derivatives for the stress fields will be transformed using the conservative form:

$$\frac{\partial u}{\partial x} = \frac{1}{J}\left(\frac{\partial}{\partial q}\left(Jq_x u\right) + \frac{\partial}{\partial r}\left(Jr_x u\right) + \frac{\partial}{\partial s}\left(Js_x u\right)\right), \tag{9}$$

and spatial derivatives for the velocity fields will be transformed using the non-conservative form:

$$\frac{\partial u}{\partial x} = q_x\frac{\partial u}{\partial q} + r_x\frac{\partial u}{\partial r} + s_x\frac{\partial u}{\partial s}. \tag{10}$$

The elastic wave equation in the transformed curvilinear coordinates is

$$\begin{pmatrix} \rho\frac{\partial v_x}{\partial t} \\ \rho\frac{\partial v_y}{\partial t} \\ \rho\frac{\partial v_z}{\partial t} \\ \mathbf{S}\begin{pmatrix} \frac{\partial \sigma_{xx}}{\partial t} \\ \frac{\partial \sigma_{yy}}{\partial t} \\ \frac{\partial \sigma_{zz}}{\partial t} \\ \frac{\partial \sigma_{xy}}{\partial t} \\ \frac{\partial \sigma_{xz}}{\partial t} \\ \frac{\partial \sigma_{yz}}{\partial t} \end{pmatrix} \end{pmatrix} = \mathcal{D}\mathbf{U}, \tag{11}$$

where

$$\mathcal{D}\mathbf{U} = \begin{pmatrix} \frac{1}{J}\left(\frac{\partial}{\partial q}\left(J\left(q_x\sigma_{xx}+q_y\sigma_{xy}+q_z\sigma_{xz}\right)\right)+\frac{\partial}{\partial r}\left(J\left(r_x\sigma_{xx}+r_y\sigma_{xy}+r_z\sigma_{xz}\right)\right)+\frac{\partial}{\partial s}\left(J\left(s_x\sigma_{xx}+s_y\sigma_{xy}+s_z\sigma_{xz}\right)\right)\right) \\ \frac{1}{J}\left(\frac{\partial}{\partial q}\left(J\left(q_x\sigma_{xy}+q_y\sigma_{yy}+q_z\sigma_{yz}\right)\right)+\frac{\partial}{\partial r}\left(J\left(r_x\sigma_{xy}+r_y\sigma_{yy}+r_z\sigma_{yz}\right)\right)+\frac{\partial}{\partial s}\left(J\left(s_x\sigma_{xy}+s_y\sigma_{yy}+s_z\sigma_{yz}\right)\right)\right) \\ \frac{1}{J}\left(\frac{\partial}{\partial q}\left(J\left(q_x\sigma_{xz}+q_y\sigma_{yz}+q_z\sigma_{zz}\right)\right)+\frac{\partial}{\partial r}\left(J\left(r_x\sigma_{xz}+r_y\sigma_{yz}+r_z\sigma_{zz}\right)\right)+\frac{\partial}{\partial s}\left(J\left(s_x\sigma_{xz}+s_y\sigma_{yz}+s_z\sigma_{zz}\right)\right)\right) \\ q_x\frac{\partial v_x}{\partial q}+r_x\frac{\partial v_x}{\partial r}+s_x\frac{\partial v_x}{\partial s} \\ q_y\frac{\partial v_y}{\partial q}+r_y\frac{\partial v_y}{\partial r}+s_y\frac{\partial v_y}{\partial s} \\ q_z\frac{\partial v_z}{\partial q}+r_z\frac{\partial v_z}{\partial r}+s_z\frac{\partial v_z}{\partial s} \\ \left(q_y\frac{\partial v_x}{\partial q}+r_y\frac{\partial v_x}{\partial r}+s_y\frac{\partial v_x}{\partial s}\right)+\left(q_x\frac{\partial v_y}{\partial q}+r_x\frac{\partial v_y}{\partial r}+s_x\frac{\partial v_y}{\partial s}\right) \\ \left(q_z\frac{\partial v_x}{\partial q}+r_z\frac{\partial v_x}{\partial r}+s_z\frac{\partial v_x}{\partial s}\right)+\left(q_x\frac{\partial v_z}{\partial q}+r_x\frac{\partial v_z}{\partial r}+s_x\frac{\partial v_z}{\partial s}\right) \\ \left(q_z\frac{\partial v_y}{\partial q}+r_z\frac{\partial v_y}{\partial r}+s_z\frac{\partial v_y}{\partial s}\right)+\left(q_y\frac{\partial v_z}{\partial q}+r_y\frac{\partial v_z}{\partial r}+s_y\frac{\partial v_z}{\partial s}\right) \end{pmatrix}. \tag{12}$$

Note that in the continuous setting, the transformed derivatives (9) and (10) are mathematically equivalent. In nontrivial geometries, discrete approximations of the transformed derivatives (9) and (10) will yield two different discrete spatial operators. Because the momentum equation defines a conservation law while Hooke's law expresses a constitutive relation, this approach is a natural way to transform the equations of linear elastodynamics. When discrete approximations are introduced, this is also crucial in order to minimize the number of floating point operations and prove numerical stability. More so, a finite difference approximation of the conservative operator (9) is more expensive than the corresponding discrete approximation of the non-conservative operator (10). The approach taken in [32,39,29,30] was to construct a skew-symmetric splitting by computing all derivatives using a weighted average of the conservative form and the non-conservative form. Evidently, when we compare our method with the approached taken in [32,39,29,30], we have reduced the expected number of floating point operations at least by half. Our approach can also be seen as a skew-symmetric splitting where certain weights have been set to 1 and others to 0, eliminating unnecessary terms and reducing numerical computations dramatically.

2.3. Boundary conditions

To define the boundary conditions, we introduce the orthonormal basis vectors $\mathbf{n} = (n_x, n_y, n_z)$, $\mathbf{m} = (m_x, m_y, m_z)$, $\mathbf{l} = (l_x, l_y, l_z)$, where $\mathbf{n}$ is the outward unit normal on the boundary. A schematic description is shown in Fig. 1.

The outward unit normal on the boundary is given by

$$\mathbf{n} = \frac{1}{\sqrt{q_x^2+q_y^2+q_z^2}}\begin{pmatrix} q_x \\ q_y \\ q_z \end{pmatrix}. \tag{13}$$

Given the unit normal $\mathbf{n}$, defined by (13), we can construct the other two basis vectors $\mathbf{m}$, $\mathbf{l}$, as follows:

$$\mathbf{m} = \frac{\mathbf{m}_0 - (\mathbf{n}^T\mathbf{m_0})\,\mathbf{n}}{|\mathbf{m}_0 - (\mathbf{n}^T\mathbf{m_0})\,\mathbf{n}|}, \quad \mathbf{l} = \mathbf{n}\times\mathbf{m}. \tag{14}$$

Here, $\mathbf{m}_0\ (\neq \pm\mathbf{n})$ is an arbitrary unit vector.

Introduce the stress tensor $\bar{\bar{\sigma}}$ and the impedance matrix $\mathbf{Z}$ defined by

$$\bar{\bar{\sigma}} = \begin{pmatrix} \sigma_{xx} & \sigma_{xy} & \sigma_{xz} \\ \sigma_{xy} & \sigma_{yy} & \sigma_{yz} \\ \sigma_{xz} & \sigma_{yz} & \sigma_{zz} \end{pmatrix}, \quad \mathbf{Z} = \begin{pmatrix} Z_n & 0 & 0 \\ 0 & Z_m & 0 \\ 0 & 0 & Z_l \end{pmatrix},$$

where $Z_n = \rho c_n$ is the p-wave impedance and $Z_m = \rho c_m$, $Z_l = \rho c_l$ are the s-wave impedances. Here, c_n, c_m, c_l are the corresponding wave-speeds determined by the eigenvalues of the matrix $\boldsymbol{\Upsilon}(n_x, n_y, n_z)$ defined in equation (4). Note that here the normalized propagation direction of the plane wave (3) is $\mathbf{n}$.

On each point on the boundary, we denote the particle velocity vector, traction vector, and the local rotation matrix on the boundary by

$$\mathbf{v} = \begin{pmatrix} v_x \\ v_y \\ v_z \end{pmatrix}, \quad \mathbf{T} = \begin{pmatrix} T_x \\ T_y \\ T_z \end{pmatrix} = \bar{\bar{\sigma}}\,\mathbf{n}, \quad \mathbf{R} = \begin{pmatrix} n_x & n_y & n_z \\ m_x & m_y & m_z \\ l_x & l_y & l_z \end{pmatrix}, \tag{15}$$

where $\det(\mathbf{R}) \neq 0$ and $\mathbf{R}^{-1} = \mathbf{R}^T$.

The corresponding in and out of the domain characteristics at the boundary are

$$\mathbf{q} = \mathbf{ZRv} + \mathbf{RT} \equiv \mathbf{Zv}^{loc} + \mathbf{T}^{loc}, \quad \mathbf{p} = \mathbf{ZRv} - \mathbf{RT} \equiv \mathbf{Zv}^{loc} - \mathbf{T}^{loc}, \tag{16}$$

where

$$\mathbf{v}^{loc} := \begin{pmatrix} v_n \\ v_m \\ v_l \end{pmatrix} = \mathbf{Rv}, \quad \mathbf{T}^{loc} := \begin{pmatrix} T_n \\ T_m \\ T_l \end{pmatrix} = \mathbf{RT}. \tag{17}$$

Note that $\mathbf{v}^{loc}$ and $\mathbf{T}^{loc}$ are the particle velocity vector and the traction vector rotated into the local orthogonal coordinates $\mathbf{n}$, $\mathbf{m}$ and $\mathbf{l}$. There are three characteristics $\mathbf{q}$ going into the domain and three characteristics $\mathbf{p}$ going out of the domain. The number of boundary conditions must correspond to the number of characteristics going into the domain, see [24,33]. We consider linear boundary conditions, the general form of the boundary conditions is

$$\mathbf{q} - \mathbf{\Gamma p} = 0 \iff \frac{1}{2}(\mathbf{I} - \mathbf{\Gamma})\,\mathbf{ZRv} + \frac{1}{2}(\mathbf{I} + \mathbf{\Gamma})\,\mathbf{RT} = 0, \tag{18}$$

where the reflection coefficient matrix $\mathbf{\Gamma}$ is real and defined by

$$\mathbf{\Gamma} = \begin{pmatrix} \gamma_n & 0 & 0 \\ 0 & \gamma_m & 0 \\ 0 & 0 & \gamma_l \end{pmatrix}, \quad 0 \le |\gamma_j| \le 1, \quad j = l, m, n.$$

The boundary conditions (18) specify the incoming characteristics $\mathbf{q}$ on the boundary in terms of the outgoing characteristics $\mathbf{p}$. Here, γ_j are the reflection coefficients. In order to simplify future algebra we have tacitly considered zero boundary data. The analysis carries over to the case of nonzero boundary data, though. We have a free-surface boundary condition if $\gamma_j = 1$, a characteristic boundary condition if $\gamma_j = 0$ and a clamped boundary condition if $\gamma_j = -1$. For later use in deriving energy estimates, we note that

$$v_j T_j = -\frac{Z_j(1-\gamma_j)}{(1+\gamma_j)} v_j^2 = -\frac{(1+\gamma_j)}{Z_j(1-\gamma_j)} T_j^2 < 0, \quad \forall |\gamma_j| < 1, \quad \text{and} \quad v_j T_j = 0, \quad \forall |\gamma_j| = 1. \tag{19}$$

2.4. Energy estimates

Here, we will derive energy estimates corresponding to the elastic wave equation (1) and (11) in a bounded domain subject to the boundary condition (18). We define the elastic energy

$$E_J(t) = \int_0^1 \int_0^1 \int_0^1 \left(\frac{\rho}{2}\left(v_x^2 + v_y^2 + v_z^2\right) + \frac{1}{2} \begin{pmatrix} \sigma_{xx} \\ \sigma_{yy} \\ \sigma_{zz} \\ \sigma_{xy} \\ \sigma_{xz} \\ \sigma_{yz} \end{pmatrix}^T \mathbf{S} \begin{pmatrix} \sigma_{xx} \\ \sigma_{yy} \\ \sigma_{zz} \\ \sigma_{xy} \\ \sigma_{xz} \\ \sigma_{yz} \end{pmatrix} \right) J dq dr ds. \tag{20}$$

By using the energy method we can show that the energy $E_J(t)$ at any time is bounded by the initial energy $E_J(0)$.

Theorem 1. *Let the basis vectors* $\mathbf{n}$, $\mathbf{m}$, $\mathbf{l}$ *be defined by* (13), (14). *The solutions of the transformed elastic wave equation* (11) *subject to the boundary condition* (18) *satisfy the energy estimate*

$$\frac{d}{dt} E_J(t) = \int_0^1 \int_0^1 (v_n T_n + v_m T_m + v_l T_l) \left(\sqrt{q_x^2 + q_y^2 + q_z^2}\, J \right) \Big|_{q=1} dr ds \le 0. \tag{21}$$

The proof of Theorem 1 follows from standard energy methods and it is concluded using the expressions in (19).

3. Fault and interface conditions

Consider now two elastic half spaces with an interface at $(\widetilde{x}(y,z), y, z)$, where $\widetilde{x}(y,z)$ is a function describing the surface of the interface. The elastic wave equation (1) is now defined on the two blocks lying to the left and right. The collocated grid points on two sides of the interface are called split nodes. We map the elastic wave equation and the curvilinear blocks to reference computational cubes. A schematic description is shown in Fig. 2. Note that we have chosen transformed coordinates such that the fault is located at the boundary $(q = 0, r, s)$.

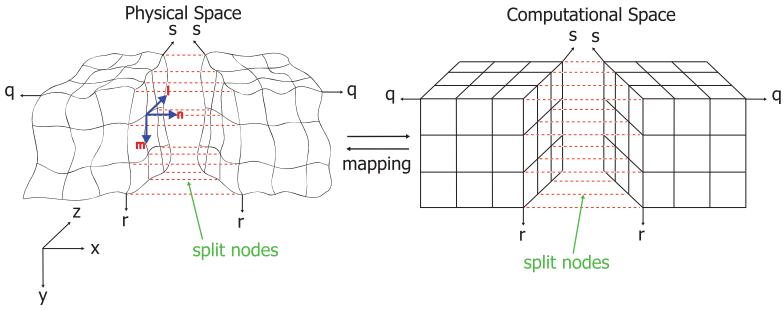

Fig. 2. Fault and boundary conforming curvilinear grids and coordinate transformation.

3.1. Friction laws

Denote the corresponding fields and material parameters with the superscripts $-/+$ for the left/right block. To define the interface conditions we rotate the particle velocity vector and the traction vector on the boundary into the local orthogonal coordinates **n**, **m**, **l** having

$$\begin{pmatrix} v_n^+ \\ v_m^+ \\ v_l^+ \end{pmatrix} = \mathbf{R}\mathbf{v}^+, \quad \begin{pmatrix} T_n^+ \\ T_m^+ \\ T_l^+ \end{pmatrix} = \mathbf{R}\mathbf{T}^+, \quad \text{and} \quad \begin{pmatrix} v_n^- \\ v_m^- \\ v_l^- \end{pmatrix} = \mathbf{R}\mathbf{v}^-, \quad \begin{pmatrix} T_n^- \\ T_m^- \\ T_l^- \end{pmatrix} = \mathbf{R}\mathbf{T}^-. \tag{22}$$

Note that in order to simplify notations and ensure consistent sign convention we have defined

$$\mathbf{T}^{\pm} = \bar{\bar{\sigma}}^{\pm}\mathbf{n}, \tag{23}$$

where $\bar{\bar{\sigma}}^{\pm}$ is the stress tensor and **n** is the unit normal pointing into the right block. Thus, $\mathbf{T}^-$ is the traction exerted by the left block on the fault, and $-\mathbf{T}^+$ is the traction exerted by the right block on the fault.

Since there are 6 characteristics going in and out of the interface, we need exactly 6 interface conditions. We begin with force balance, obtaining relations on the tractions acting on the interface:

$$\mathbf{T}^- = \mathbf{T}^+ \iff T_j^+ = T_j^- = T_j, \quad j = l, m, n. \tag{24}$$

To specify the remaining three conditions we define jumps on the velocities:

$$[\![v_j]\!] = v_j^+ - v_j^-, \quad j = l, m, n.$$

We assume that there is no opening or interpenetration of the two sides. Thus the opening velocity is zero,

$$[\![v_n]\!] = 0. \tag{25}$$

The slip rate and the shear strength on the fault are defined by

$$V = \sqrt{[\![v_m]\!]^2 + [\![v_l]\!]^2}, \quad \tau = \sqrt{T_m^2 + T_l^2}. \tag{26}$$

Slip S is defined as the discontinuity in the tangential displacement fields, $dS/dt = V$. The slip rate and the shear stress on the fault are related via

$$T_l = \sigma_n \frac{f(V,\psi)}{V}[\![v_l]\!], \quad T_m = \sigma_n \frac{f(V,\psi)}{V}[\![v_m]\!]. \tag{27}$$

Here, ψ is a state variable and the compressive normal stress σ_n is defined by

$$\sigma_n = \max(0, -T_n). \tag{28}$$

The state variable ψ is governed by an ordinary differential equation

$$\frac{d\psi}{dt} = G(V,\psi). \tag{29}$$

Note that (27) implies that the shear traction vector and the slip velocity are parallel

$$\frac{T_l}{\tau} = \frac{[\![v_l]\!]}{V}, \quad \frac{T_m}{\tau} = \frac{[\![v_m]\!]}{V}, \tag{30}$$

and the shear strength on the fault is constrained by the nonlinear friction law

$$\tau = \sigma_n f(V,\psi) \geq 0. \tag{31}$$

In general, $f(V,\psi,)$ and $G(V,\psi)$ are highly nonlinear functions with $f(0,\psi) = 0$ for all ψ.

3.2. Energy dissipation rate

For reference purpose we summarize the interface conditions:

$$\text{Force balance:} \quad T_n^+ = T_n^-, \quad T_m^+ = T_m^-, \quad T_l^+ = T_l^-, \tag{32a}$$

$$\text{No opening:} \quad [\![v_n]\!] = 0, \tag{32b}$$

$$\text{Friction law:} \quad T_m = \sigma_n \frac{f(V,\psi)}{V}[\![v_m]\!], \quad T_l = \sigma_n \frac{f(V,\psi)}{V}[\![v_l]\!]. \tag{32c}$$

We will show that the interface condition (32) dissipates the total elastic energy. In particular we can prove the theorem:

Theorem 2. *Let $E_J^{\pm}$ denote the elastic energy in the $\pm$-sides of the fault. If $f(V,\psi)\,V \geq 0$, then the sum of the energies satisfies*

$$\frac{d}{dt}\left(E_J^- + E_J^+\right) = -\int_0^1\int_0^1 \sigma_n f(V,\psi)\, V \left(J\sqrt{q_x^2+q_y^2+q_z^2}\right)\Big|_{q=0} drds \leq 0. \tag{33}$$

In particular if the interface is locked, $V = 0$, the total energy is conserved,

$$\frac{d}{dt}\left(E_J^- + E_J^+\right) = 0. \tag{34}$$

Remark 2. Theorem 2 alone does not guarantee well-posedness of the corresponding IBVP [33]. In order to guarantee well-posedness, in addition to Theorem 2, a unique solution must exist. However, the proof of well-posedness of IBVPs resulting from nonlinear friction laws (32) is beyond the scope of this paper. Here, we assume that the friction laws together with the elastic wave equation is well-posed, and focus our attention on developing a stable numerical method for those models. Numerical stability will be demonstrated by deriving discrete energy estimates analogous to (33), (34).

3.3. The stress transfer functional and hat-functions

The difficulty lies in constructing stable discrete approximations and deriving discrete energy estimates, analogous to (33) and (34), without introducing additional numerical stiffness. To succeed, we construct a subspace of functions (solutions) satisfying the elastic wave equation and the interface conditions (32), and then project the particle velocities and tractions on the fault to that subspace.

Assume that the particle velocities $(v_x, v_y, v_z)^T$ and the stress field $(\sigma_{xx}, \sigma_{yy}, \sigma_{zz}, \sigma_{xy}, \sigma_{xz}, \sigma_{yz})^T$ satisfy the elastic wave equation (11). Define the characteristics propagating to the fault

$$p_j^- = Z_j^- v_j^- - T_j^-, \quad q_j^+ = Z_j^+ v_j^+ + T_j^+, \quad j = l, m, n \tag{35}$$

where $Z_j^{\pm}$ are the impedances. Using (32a) and (35), we can now write

$$T_j = \Phi_j - \eta_j [\![v_j]\!], \tag{36}$$

where

$$\Phi_j = \eta_j\left(\frac{1}{Z_j^+}q_j^+ - \frac{1}{Z_j^-}p_j^-\right), \quad \eta_j = \frac{Z_j^+ Z_j^-}{Z_j^+ + Z_j^-}. \tag{37}$$

Note that the representation (36) embodies the elastic wave equation and force balance on the fault (32a), and arises naturally in boundary integral equation formulations of elastodynamics [22]. Here, Φ_j are called the stress transfer functionals and $\eta_j[\![v_j]\!]$ are called the radiation damping terms [48,47,45,46]. The stress transfer functionals Φ_j are tractions on a locked fault $[\![v_j]\!] = 0$, which are altered by outgoing wave radiation when the fault is slipping $[\![v_j]\!] \neq 0$.

We define the hat-functions satisfying

$$\widehat{q}_j^+ := Z_j^+ \widehat{v}_j^+ + \widehat{T}_j^+ = q_j^+ = Z_j^+ v_j^+ + T_j^+, \tag{38a}$$

$$\widehat{p}_j^- := Z_j^- \widehat{v}_j^- - \widehat{T}_j^- = p_j^- = Z_j^- v_j^- - T_j^-, \tag{38b}$$

and the interface condition (32) exactly. Given q_j^+, p_j^-, the procedure will solve (38) and (32) for the hat-functions, $\widehat{v}_j^{\pm}, \widehat{T}_j^{\pm}$. As before, we use force balance and the stress transfer functionals to rewrite (38) and (32), having

$$\text{Force balance:} \quad \widehat{T}_n + \eta_n[\![\widehat{v}_n]\!] = \Phi_n, \quad \widehat{T}_m + \eta_m[\![\widehat{v}_m]\!] = \Phi_m, \quad \widehat{T}_l + \eta_l[\![\widehat{v}_l]\!] = \Phi_l, \tag{39a}$$

$$\text{No opening:} \quad [\![\widehat{v}_n]\!] = 0, \tag{39b}$$

$$\text{Friction law:} \quad \widehat{T}_m = \widehat{\sigma}_n \frac{f(\widehat{V},\psi)}{\widehat{V}}[\![\widehat{v}_m]\!], \quad \widehat{T}_l = \widehat{\sigma}_n \frac{f(\widehat{V},\psi)}{\widehat{V}}[\![\widehat{v}_l]\!], \tag{39c}$$

where

$$\widehat{V} = \sqrt{[\![\widehat{v}_m]\!]^2 + [\![\widehat{v}_l]\!]^2}.$$

We need to solve equation (39) for the hat-functions corresponding to tractions $\widehat{T}_j$ and jump in particle velocities $[\![\widehat{v}_j]\!]$. In the normal direction $j = n$, we have closed form solutions

$$[\![\widehat{v}_n]\!] = 0, \quad \widehat{T}_n = \Phi_n,$$

thus, implying

$$\widehat{\sigma}_n = \max\left(0, -\widehat{T}_n\right).$$

In the tangential directions we have four coupled algebraic equations to solve,

$$\widehat{T}_m + \eta_m [\![\widehat{v}_m]\!] = \Phi_m, \quad \widehat{T}_l + \eta_l [\![\widehat{v}_l]\!] = \Phi_l, \tag{40a}$$

$$\widehat{T}_m = \widehat{\sigma}_n \frac{f\left(\widehat{V}, \psi\right)}{\widehat{V}} [\![\widehat{v}_m]\!], \quad \widehat{T}_l = \widehat{\sigma}_n \frac{f\left(\widehat{V}, \psi\right)}{\widehat{V}} [\![\widehat{v}_l]\!]. \tag{40b}$$

However, we can reduce the algebraic problem (40) to two nonlinear equations for hat-functions corresponding to slip velocities, $[\![\widehat{v}_l]\!]$, $[\![\widehat{v}_m]\!]$.

$$[\![\widehat{v}_m]\!] = \left(\eta_m + \widehat{\sigma}_n \frac{f\left(\widehat{V}, \psi\right)}{\widehat{V}}\right)^{-1} \Phi_m, \quad [\![\widehat{v}_l]\!] = \left(\eta_l + \widehat{\sigma}_n \frac{f\left(\widehat{V}, \psi\right)}{\widehat{V}}\right)^{-1} \Phi_l. \tag{41}$$

The nonlinear problems (41) can be reduced further to a single equation for the hat-function corresponding to slip rate

$$\sqrt{\left(\eta_l \widehat{V} + \widehat{\sigma}_n f\left(\widehat{V}, \psi\right)\right)^{-2} \Phi_l^2 + \left(\eta_m \widehat{V} + \widehat{\sigma}_n f\left(\widehat{V}, \psi\right)\right)^{-2} \Phi_m^2} = 1. \tag{42}$$

Note that in an isotropic medium we have $\eta_l = \eta_m = \eta$, thus yielding

$$\eta \widehat{V} + \widehat{\sigma}_n f\left(\widehat{V}, \psi\right) = \sqrt{\Phi_l^2 + \Phi_m^2}. \tag{43}$$

We can now solve (42) or (43) to determine the hat-function for the slip rate $\widehat{V}$, and then evaluate (41) to compute the hat-functions corresponding to the slip velocities. After computing the hat-functions corresponding to slip velocities $[\![\widehat{v}_l]\!]$, $[\![\widehat{v}_m]\!]$ in (41), we can obtain the hat-functions corresponding to shear tractions $\widehat{T}_l$, $\widehat{T}_m$ directly from (40). We can now define explicitly the hat-functions corresponding to the particle velocities

$$\widehat{v}_j^+ = \frac{p_j^- + \widehat{T}_j}{Z_j^-} + [\![\widehat{v}_j]\!], \quad \widehat{v}_j^- = \frac{q_j^+ - \widehat{T}_j}{Z_j^+} - [\![\widehat{v}_j]\!]. \tag{44}$$

Note that we have equivalently redefined the fault/interface condition (32) as follows

$$v_j^\pm = \widehat{v}_j^\pm, \quad T_j^- = T_j^+ = \widehat{T}_j, \quad j = l, m, n. \tag{45}$$

In particular, (45) defines a rule to update particle velocities and tractions on the fault.

Remark 3. One may be concerned if (42) or (43) always has a unique solution (or even a solution). Note that if the IBVP corresponding to the interface condition (32) is well-posed, then there is a unique solution of the IBVP and by construction the solution satisfies (42) or (43). Further, if $f(0, \psi) = 0$ and $\partial f(V, \psi)/\partial V \geq 0$, then using a geometric argument we can show that the solution of (42) or (43) is unique. Therefore, using our constructions, the solutions of the IBVP are the only solutions to (42) or (43). We remark also that many friction laws used in dynamic earthquake rupture simulations satisfy the requirements $f(0, \psi) = 0$ and $\partial f(V, \psi)/\partial V \geq 0$.

We can now formulate a result equivalent to Theorem 2.

Theorem 3. *Let $E_J^\pm$ denote the elastic energy in the $\pm$-sides of the fault. If the fault/interface condition is determined by (45), that is $v_j^\pm = \widehat{v}_j^\pm$, $T_j^- = T_j^+ = \widehat{T}_j$ $(j = l, m, n)$ on the fault, then the sum of the energies satisfies*

$$\frac{d}{dt}\left(E_J^- + E_J^+\right) = -\int_0^1 \int_0^1 \widehat{\sigma}_n f\left(\widehat{V}, \psi\right) \widehat{V} \left(J\sqrt{q_x^2 + q_y^2 + q_z^2}\right)\Big|_{q=0} drds \leq 0. \tag{46}$$

4. Stable numerical approximations

In this section, we introduce discrete approximations and prove numerical stability. We will use SBP finite difference operators to approximate all spatial derivatives and impose boundary and interface conditions weakly using penalties. In order to prove numerical stability we will derive discrete energy estimates analogous to (21) and (46).

4.1. Spatial discrete operators

Consider the uniform discretization of the unit interval, $0 \le q \le 1$, with N_q number of grid points and the spatial step, $h_q > 0$,

$$q_i = (i-1)\,h_q, \quad i = 1, 2, \ldots, N_q, \quad h_q = \frac{1}{N_q - 1}. \tag{47}$$

Let D_q be a differentiation matrix approximating the first derivative, $D_q \approx \partial/\partial q$, on the uniform grid (47). The matrix D_q is an SBP operator (in one space dimension), if the following properties hold

$$D_q = \mathrm{H}_q^{-1} Q_q, \quad Q_q^T + Q_q = E_{Rq} - E_{Lq}, \quad \mathrm{H}_q = \mathrm{H}_q^T > 0. \tag{48}$$

Here, $E_{Lq} = \mathrm{diag}(1, 0, 0, \ldots, 0)$, $E_{Rq} = \mathrm{diag}(0, 0, 0, \ldots, 1)$ pick out the left and right boundary values. The matrix H_q is diagonal with positive entries $h_{ii}^{(q)} > 0$, thus defining a discrete norm. The matrix Q_q is almost skew-symmetric. Note that from the SBP property (48) we have

$$D_q = \mathrm{H}_q^{-1} Q_q = \mathrm{H}_q^{-1} \left(-\left(\mathrm{H}_q^{-1} Q_q\right)^T \mathrm{H}_q + E_{Rq} - E_{Lq} \right) = -\mathrm{H}_q^{-1} D_q^T \mathrm{H}_q + \mathrm{H}_q^{-1} \left(E_{Rq} - E_{Lq} \right). \tag{49}$$

The SBP finite difference operator D_q defined in (48) mimics the integration-by-parts property of the continuous operator. This is crucial in order to prove numerical stability. The SBP operator used in this study can be found in [23].

4.2. Discretization of the three space dimensional elastic wave equation

We discretize the spatial domain in the q-, r-, and s-directions using N_q, N_r, N_s grid points with constant spatial steps h_q, h_r, h_s, respectively. A three space dimensional scalar grid function, $\mathbf{u} = [u_{ijk}]$, is stacked as a vector of length $N_q N_r N_s$, $\mathbf{u} = \left(u_{111}, u_{112}, \ldots, u_{N_q N_r N_s}\right)^T$. All three space dimensional scalar material parameters are rearranged as diagonal matrices of the form $\mathbf{a} = \mathrm{diag}\left(a_{111}, a_{112}, \ldots, a_{N_q N_r N_s}\right)$. Spatial derivatives in higher space dimensions are derived using the Kronecker products,

$$\mathbf{D}_q = \left(D_q \otimes I_r \otimes I_s\right), \quad \mathbf{D}_r = \left(I_q \otimes D_r \otimes I_s\right), \quad \mathbf{D}_s = \left(I_q \otimes I_r \otimes D_s\right).$$

Here, D_q, D_r, D_s are one space dimensional SBP operators and I_q, I_r, I_s are identity matrices of sizes corresponding to the number of grid points N_q, N_r, N_s.

We use the SBP operators to compute the metric derivatives, that is $\mathbf{x}_q = \mathbf{D}_q \mathbf{x}$, $\mathbf{y}_r = \mathbf{D}_r \mathbf{y}$, $\mathbf{z}_s = \mathbf{D}_s \mathbf{z}$, $\ldots$, where $(\mathbf{x}, \mathbf{y}, \mathbf{z})$ denote the curvilinear mesh. The conservative transformation (9) is approximated by

$$\frac{\partial u}{\partial x} \approx \mathbf{J}^{-1} \left(\mathbf{D}_q \left(\mathbf{J} \mathbf{q}_x \mathbf{u} \right) + \mathbf{D}_r \left(\mathbf{J} \mathbf{r}_x \mathbf{u} \right) + \mathbf{D}_s \left(\mathbf{J} \mathbf{s}_x \mathbf{u} \right) \right), \tag{50}$$

and the non-conservative transformation (10) is approximated by

$$\frac{\partial u}{\partial x} \approx \mathbf{q}_x \mathbf{D}_q \mathbf{u} + \mathbf{r}_x \mathbf{D}_r \mathbf{u} + \mathbf{s}_x \mathbf{D}_s \mathbf{u}. \tag{51}$$

If $u = const$, a constant function, then any derivative of u must vanish, $\frac{\partial u}{\partial x} \equiv 0$, independent of the mesh. For a constant function, the non-conservative approximation (51) also vanishes completely independent of the mesh. For the conservative approximation (50) we have

$$\mathbf{u}_x = u \mathbf{J}^{-1} \left(\mathbf{D}_q \left(\mathbf{J} \mathbf{q}_x \right) + \mathbf{D}_r \left(\mathbf{J} \mathbf{r}_x \right) + \mathbf{D}_s \left(\mathbf{J} \mathbf{s}_x \right) \right). \tag{52}$$

If the metric terms are determined by (7), then for a constant function on a general mesh, from (52) we have $\mathbf{u}_x = O\left(h^p\right)$, where p is the order of accuracy of the SBP operator. Note that $\mathbf{u}_x = O\left(h^p\right)$ will vanish asymptotically with mesh refinement at the rate p. However, if we use the representation (8), then from (52) we have $\mathbf{u}_x \equiv 0$, on any mesh. The preservation of the derivative of a constant function can be useful in ensuring accuracy for nonlinear problems, see for instance the *free-stream preservation* [28,57] in computational fluid dynamics. However, for wave propagation in linear elastic media, as long as the numerical method is stable, we have not found this to be an issue.

The semi-discrete approximation of the elastic wave equation (11) is

$$\begin{pmatrix} \rho\frac{d\mathbf{v}_x}{dt} \\ \rho\frac{d\mathbf{v}_y}{dt} \\ \rho\frac{d\mathbf{v}_z}{dt} \\ \mathbf{S}\begin{pmatrix} \frac{d\sigma_{xx}}{dt} \\ \frac{d\sigma_{yy}}{dt} \\ \frac{d\sigma_{zz}}{dt} \\ \frac{d\sigma_{xy}}{dt} \\ \frac{d\sigma_{xz}}{dt} \\ \frac{d\sigma_{yz}}{dt} \end{pmatrix} \end{pmatrix} = \mathbf{DU}, \tag{53}$$

where the discrete spatial operator $\mathbf{D}$ is defined by

$$\mathbf{DU} = \begin{pmatrix} \mathbf{J}^{-1}\left(\mathbf{D}_q\left(\mathbf{J}\left(\mathbf{q}_x\sigma_{xx}+\mathbf{q}_y\sigma_{xy}+\mathbf{q}_z\sigma_{xz}\right)\right)+\mathbf{D}_r\left(\mathbf{J}\left(\mathbf{r}_x\sigma_{xx}+\mathbf{r}_y\sigma_{xy}+\mathbf{r}_z\sigma_{xz}\right)\right)+\mathbf{D}_s\left(\mathbf{J}\left(\mathbf{s}_x\sigma_{xx}+\mathbf{s}_y\sigma_{xy}+\mathbf{s}_z\sigma_{xz}\right)\right)\right) \\ \mathbf{J}^{-1}\left(\mathbf{D}_q\left(\mathbf{J}\left(\mathbf{q}_x\sigma_{xy}+\mathbf{q}_y\sigma_{yy}+\mathbf{q}_z\sigma_{yz}\right)\right)+\mathbf{D}_r\left(\mathbf{J}\left(\mathbf{r}_x\sigma_{xy}+\mathbf{r}_y\sigma_{yy}+\mathbf{r}_z\sigma_{yz}\right)\right)+\mathbf{D}_s\left(\mathbf{J}\left(\mathbf{s}_x\sigma_{xy}+\mathbf{s}_y\sigma_{yy}+\mathbf{s}_z\sigma_{yz}\right)\right)\right) \\ \mathbf{J}^{-1}\left(\mathbf{D}_q\left(\mathbf{J}\left(\mathbf{q}_x\sigma_{xz}+\mathbf{q}_y\sigma_{yz}+\mathbf{q}_z\sigma_{zz}\right)\right)+\mathbf{D}_r\left(\mathbf{J}\left(\mathbf{r}_x\sigma_{xz}+\mathbf{r}_y\sigma_{yz}+\mathbf{r}_z\sigma_{zz}\right)\right)+\mathbf{D}_s\left(\mathbf{J}\left(\mathbf{s}_x\sigma_{xz}+\mathbf{s}_y\sigma_{yz}+\mathbf{s}_z\sigma_{zz}\right)\right)\right) \\ \mathbf{q}_x\mathbf{D}_q\mathbf{v}_x+\mathbf{r}_x\mathbf{D}_r\mathbf{v}_x+\mathbf{s}_x\mathbf{D}_s\mathbf{v}_x \\ \mathbf{q}_y\mathbf{D}_q\mathbf{v}_y+\mathbf{r}_y\mathbf{D}_r\mathbf{v}_y+\mathbf{s}_y\mathbf{D}_s\mathbf{v}_y \\ \mathbf{q}_z\mathbf{D}_q\mathbf{v}_z+\mathbf{r}_z\mathbf{D}_r\mathbf{v}_z+\mathbf{s}_z\mathbf{D}_s\mathbf{v}_z \\ \mathbf{q}_y\mathbf{D}_q\mathbf{v}_x+\mathbf{r}_y\mathbf{D}_r\mathbf{v}_x+\mathbf{s}_y\mathbf{D}_s\mathbf{v}_x+\mathbf{q}_x\mathbf{D}_q\mathbf{v}_y+\mathbf{r}_x\mathbf{D}_r\mathbf{v}_y+\mathbf{s}_x\mathbf{D}_s\mathbf{v}_y \\ \mathbf{q}_z\mathbf{D}_q\mathbf{v}_x+\mathbf{r}_z\mathbf{D}_r\mathbf{v}_x+\mathbf{s}_z\mathbf{D}_s\mathbf{v}_x+\mathbf{q}_x\mathbf{D}_q\mathbf{v}_z+\mathbf{r}_x\mathbf{D}_r\mathbf{v}_z+\mathbf{s}_x\mathbf{D}_s\mathbf{v}_z \\ \mathbf{q}_z\mathbf{D}_q\mathbf{v}_y+\mathbf{r}_z\mathbf{D}_r\mathbf{v}_y+\mathbf{s}_z\mathbf{D}_s\mathbf{v}_y+\mathbf{q}_y\mathbf{D}_q\mathbf{v}_z+\mathbf{r}_y\mathbf{D}_r\mathbf{v}_z+\mathbf{s}_y\mathbf{D}_s\mathbf{v}_z \end{pmatrix}. \tag{54}$$

4.3. Boundary treatments

Next, we enforce the boundary condition (18). For more compact notations we introduce $\mathbf{H}_{qrs} = \left(I_9 \otimes H_q \otimes H_r \otimes H_s\right)$, $\mathbf{J}_{qrs} = (I_9 \otimes \mathbf{J})$, $\mathbf{E} = \left(I_9 \otimes E_{Rq} \otimes I_r \otimes I_s\right)$. The boundary conditions (18) are imposed weakly using SAT. That is we construct a forcing function satisfying the boundary condition and add it to the right hand side of (53) with special penalty weights. The semi-discrete approximation of the elastic wave equation (11) with a weak enforcement of the boundary conditions (18) is

$$\begin{pmatrix} \rho\frac{d\mathbf{v}_x}{dt} \\ \rho\frac{d\mathbf{v}_y}{dt} \\ \rho\frac{d\mathbf{v}_z}{dt} \\ \mathbf{S}\begin{pmatrix} \frac{d\sigma_{xx}}{dt} \\ \frac{d\sigma_{yy}}{dt} \\ \frac{d\sigma_{zz}}{dt} \\ \frac{d\sigma_{xy}}{dt} \\ \frac{d\sigma_{xz}}{dt} \\ \frac{d\sigma_{yz}}{dt} \end{pmatrix} \end{pmatrix} = \mathbf{DU} - \left(I_9 \otimes H_q^{-1} \otimes I_r \otimes I_s\right)\mathbf{E}\sqrt{\mathbf{q}_x^2+\mathbf{q}_y^2+\mathbf{q}_z^2}\begin{pmatrix} \alpha_x\mathbf{F}_x \\ \alpha_y\mathbf{F}_y \\ \alpha_z\mathbf{F}_z \\ \theta_x n_x\widetilde{\mathbf{F}}_x \\ \theta_y n_y\widetilde{\mathbf{F}}_y \\ \theta_z n_z\widetilde{\mathbf{F}}_z \\ \theta_x n_y\widetilde{\mathbf{F}}_x+\theta_y n_x\widetilde{\mathbf{F}}_y \\ \theta_x n_z\widetilde{\mathbf{F}}_x+\theta_z n_x\widetilde{\mathbf{F}}_z \\ \theta_y n_z\widetilde{\mathbf{F}}_y+\theta_z n_y\widetilde{\mathbf{F}}_z \end{pmatrix}, \tag{55}$$

where $\mathbf{F}$, $\widetilde{\mathbf{F}}$ are the SAT forcing defined by

$$\begin{aligned} \mathbf{F} &\equiv \frac{1}{2}\mathbf{R}^T\left(\mathbf{I}-\mathbf{\Gamma}\right)\mathbf{Z}\mathbf{R}\mathbf{v} + \frac{1}{2}\mathbf{R}^T\left(\mathbf{I}+\mathbf{\Gamma}\right)\mathbf{R}\mathbf{T}, \\ \widetilde{\mathbf{F}} &\equiv \mathbf{R}^T\mathbf{Z}^{-1}\mathbf{R}\mathbf{F} = \frac{1}{2}\mathbf{R}^T\left(\mathbf{I}-\mathbf{\Gamma}\right)\mathbf{R}\mathbf{v} + \frac{1}{2}\mathbf{R}^T\left(\mathbf{I}+\mathbf{\Gamma}\right)\mathbf{Z}^{-1}\mathbf{R}\mathbf{T}. \end{aligned} \tag{56}$$

The matrix $\mathbf{E}$ projects the SAT forcing on the boundaries, and if the boundary condition (18) is satisfied exactly then we have $\mathbf{F} \equiv 0$ and $\widetilde{\mathbf{F}} \equiv 0$. Here, n_x, n_y, n_z are the components of the outward unit vector $\mathbf{n}$. The dimensionless real numbers α_x, α_y, α_z and θ_x, θ_y, θ_z are penalty parameters determined by requiring stability. We also remark that the SAT forcing functions $\mathbf{F}$ and $\widetilde{\mathbf{F}}$ are invariant with coordinate rotation $\mathbf{R}$.

4.4. Discrete stability of the boundary treatments

Here, we prove the numerical stability of the boundary treatment (55). The aim is to derive sharp estimates of the penalty parameters α_x, α_y, α_z and θ_x, θ_y, θ_z, and a corresponding discrete energy estimate analogous to (21). To begin with, we approximate the elastic energy (20) by a quadrature rule

$$\mathbf{E}_{Jh} = \sum_{k=1}^{N_s}\sum_{j=1}^{N_r}\sum_{i=1}^{N_q}\left(\frac{\rho_{ijk}}{2}\left(v_{xijk}^2 + v_{yijk}^2 + v_{zijk}^2\right) + \frac{1}{2}\begin{pmatrix}\sigma_{xxijk}\\ \sigma_{yyijk}\\ \sigma_{zzijk}\\ \sigma_{xyijk}\\ \sigma_{xzijk}\\ \sigma_{yzijk}\end{pmatrix}^T \mathbf{S}_{ijk}\begin{pmatrix}\sigma_{xxijk}\\ \sigma_{yyijk}\\ \sigma_{zzijk}\\ \sigma_{xyijk}\\ \sigma_{xzijk}\\ \sigma_{yzijk}\end{pmatrix}\right) J_{ijk}h_{ii}^{(q)}h_{jj}^{(r)}h_{kk}^{(s)}. \tag{57}$$

Note that for all SBP operators considered in this study, the quadrature weights are positive $h_{ii}^{(q)}, h_{jj}^{(r)}, h_{kk}^{(s)} > 0$. Therefore, the discrete quantity $\mathbf{E}_{Jh}$ defined in (57) is a discrete elastic energy. If the solutions of the discrete equation (55) satisfy $\mathbf{E}_{Jh}(t) \leq \mathbf{E}_{Jh}(0)$ for all $t \geq 0$, then we say that the numerical approximation is asymptotically stable. We can now state a main result

Theorem 4 *(General case). Consider the semi-discrete approximation (55) of the elastic wave equation subject to the boundary condition (18). If $\alpha_x = \alpha_y = \alpha_z = 1$, $\theta_x = \theta_y = \theta_z = 1$, then*

$$\frac{d}{dt}\mathbf{E}_{Jh} \leq 0.$$

The semi-discrete approximation (55) is asymptotically stable.

Proof. Multiply equation (55) by $\left(\mathbf{v}_x, \mathbf{v}_y, \mathbf{v}_z, \sigma_{xx}, \sigma_{yy}, \sigma_{zz}, \sigma_{xy}, \sigma_{xz}, \sigma_{yz}\right)\mathbf{H}_{qrs}\mathbf{J}_{qrs}$ from the left and use the SBP property (48) or (49) for the momentum equations (the first three equations in (55)) only. The interior terms cancel out. By ignoring the boundary terms at $i = 1,\ j = 1,\ N_r,\ k = 1, N_s$ and introducing $|\mathbf{q}_{Njk}| = \sqrt{q_{xN_qjk}^2 + q_{yN_qjk}^2 + q_{zN_qjk}^2}$ we have

$$\frac{d}{dt}\mathbf{E}_{Jh} = -\sum_{i=l,m,n}\sum_{k=1}^{N_s}\sum_{j=1}^{N_r}\frac{|\mathbf{q}_{Njk}|}{2}\left(Z_i\left(1-\gamma_i\right)v_i^2 + \frac{\left(1+\gamma_i\right)}{Z_i}T_i^2\right)J_{N_qjk}h_{jj}^{(r)}h_{kk}^{(s)}. \tag{58}$$

Note that all terms in the right hand side above are negative semi-definite, thus we have

$$\frac{d}{dt}\mathbf{E}_{Jh} \leq 0.$$

Therefore, the semi-discrete approximation (55) is asymptotically stable. □

Note that the boundary treatment (55), with $\alpha_j = \theta_j = 1$, dissipates energy at least as fast as the continuous problem. Take for instance the case of a free-surface boundary condition with $\gamma_j = 1$. From (58) we have

$$\frac{d}{dt}\mathbf{E}_{Jh} = -\sum_{i=l,m,n}\sum_{k=1}^{N_s}\sum_{j=1}^{N_r}|\mathbf{q}_{Njk}|\frac{1}{Z_i}T_i^2 J_{N_qjk}h_{jj}^{(r)}h_{kk}^{(s)}. \tag{59}$$

The terms in the right hand side of (59) are dissipative. Since (55) is a consistent approximation and tractions are expected to be zero, $T_j = 0$, in the limit of mesh refinement these artificial dissipative terms will vanish.

For some boundary conditions it may be more beneficial to penalize only certain equations in (55). This has the potential to minimize artificial numerical dissipation.

Theorem 5 *(No numerical dissipation). Consider the semi-discrete approximation (55) of the elastic wave equation subject to the boundary conditions (18). The following results are true*

- *A free-surface boundary: If $\gamma_j = 1$ $(j = l, m, n)$ and $\alpha_x = \alpha_y = \alpha_z = 1$, $\theta_x = \theta_x = \theta_z = 0$, then the solutions of the discrete equation (55) satisfy the energy conservation equation*

$$\frac{d}{dt}\mathbf{E}_{Jh} = 0. \tag{60}$$

- *A velocity boundary: If* $\gamma_j = -1$ *(*$j = l, m, n$*) and* $\alpha_x = \alpha_y = \alpha_z = 0$, $\theta_x = \theta_x = \theta_z = 1$ *then the solutions of the discrete equation (55) satisfy the energy conservation equation*

$$\frac{d}{dt}\mathbf{E}_{Jh} = 0. \tag{61}$$

- *An absorbing boundary: If* $\gamma_j = 0$ *(*$j = l, m, n$*) then*
  a) *with* $\alpha_x = \alpha_y = \alpha_z = 2$, $\theta_x = \theta_x = \theta_z = 0$, *the solutions of the discrete equation (55) satisfy the energy equation*

$$\frac{d}{dt}\mathbf{E}_{Jh} = -\sum_{i=l,m,n}\sum_{k=1}^{N_s}\sum_{j=1}^{N_r} |\mathbf{q}_{Njk}| Z_i v_i^2 J_{N_q jk} h_{jj}^{(r)} h_{kk}^{(s)}, \tag{62}$$

  or
  b) *with* $\alpha_x = \alpha_y = \alpha_z = 0$, $\theta_x = \theta_x = \theta_z = 2$ *the solutions of the discrete equation (55) satisfy the energy equation*

$$\frac{d}{dt}\mathbf{E}_{Jh} = -\sum_{i=l,m,n}\sum_{k=1}^{N_s}\sum_{j=1}^{N_r} |\mathbf{q}_{Njk}| \frac{1}{Z_i} T_i^2 J_{N_q jk} h_{jj}^{(r)} h_{kk}^{(s)}. \tag{63}$$

We will omit the proof of Theorem 5 since it is analogous to the proof of Theorem 4. Note that the energy equations (60)–(63) are in full accordance with the PDE and the boundary conditions. That is, there is no artificial numerical dissipation.

4.5. Interface treatment for friction laws

We present now the numerical interface treatments for friction laws. The interface procedure begins with the construction of the hat variables, as outlined in Section 3.3. The major difference here is that the hat-functions and the stress transfer functionals are computed using the semi-discrete grid functions, instead of the continuous functions used in Section 3.3. For nonlinear friction laws the hat-functions for slip rate are computed, from the relation (42) or (43), using a nonlinear solver such as Newton–Raphson. We also remark that the hat-functions $\widehat{v}_j^{\pm}$, $\widehat{T}_j^{\pm}$ are computed in the l, m, n coordinates, but they can be rotated back to the x, y, z coordinates using the transformation

$$\widehat{\mathbf{v}}^{\pm} = \mathbf{R}^T \begin{pmatrix} \widehat{v}_n^{\pm} \\ \widehat{v}_m^{\pm} \\ \widehat{v}_l^{\pm} \end{pmatrix}, \quad \widehat{\mathbf{T}}^{\pm} = \mathbf{R}^T \begin{pmatrix} \widehat{T}_n^{\pm} \\ \widehat{T}_m^{\pm} \\ \widehat{T}_l^{\pm} \end{pmatrix}. \tag{64}$$

We could now update velocities and tractions on the fault by using

$$\mathbf{v}^{\pm} = \widehat{\mathbf{v}}^{\pm}, \quad \mathbf{T}^{\pm} = \widehat{\mathbf{T}}^{\pm}. \tag{65}$$

However, in order to ensure numerical stability we will enforce the discretized interface condition (65) weakly using penalties. We begin by constructing the SAT forcing

$$\begin{aligned} \mathbf{F}^{\pm} &\equiv \frac{1}{2}\mathbf{R}^T \mathbf{Z}^{\pm} \mathbf{R} \left(\mathbf{v}^{\pm} - \widehat{\mathbf{v}}^{\pm}\right) \mp \frac{1}{2}\left(\mathbf{T}^{\pm} - \widehat{\mathbf{T}}^{\pm}\right), \\ \widetilde{\mathbf{F}}^{\pm} &\equiv \mathbf{R}^T \left(\mathbf{Z}^{\pm}\right)^{-1} \mathbf{R}\mathbf{F}^{\pm} = \frac{1}{2}\left(\mathbf{v}^{\pm} - \widehat{\mathbf{v}}^{\pm}\right) \mp \frac{1}{2}\mathbf{R}^T \left(\mathbf{Z}^{\pm}\right)^{-1} \mathbf{R}\left(\mathbf{T}^{\pm} - \widehat{\mathbf{T}}^{\pm}\right). \end{aligned} \tag{66}$$

Note that if the interface conditions (65) are satisfied exactly, that is $\mathbf{v}^{\pm} = \widehat{\mathbf{v}}^{\pm}$, $\mathbf{T}^{\pm} = \widehat{\mathbf{T}}^{\pm}$, then the SAT forcing functions will vanish completely, $\mathbf{F}^{-} = \mathbf{F}^{+} = \widetilde{\mathbf{F}}^{-} = \widetilde{\mathbf{F}}^{+} = 0$. Note also that the interface SAT forcing functions (66) are invariant with coordinate rotation $\mathbf{R}$.

Then, we append the forcing functions defined in (66) to the right hand side of (53) with special penalty parameters, obtaining

$$\begin{pmatrix} \rho\frac{d\mathbf{v}_x^{\pm}}{dt} \\ \rho\frac{d\mathbf{v}_y^{\pm}}{dt} \\ \rho\frac{d\mathbf{v}_z^{\pm}}{dt} \\ \mathbf{S}^{\pm}\begin{pmatrix} \frac{d\sigma_{xx}^{\pm}}{dt} \\ \frac{d\sigma_{yy}^{\pm}}{dt} \\ \frac{d\sigma_{zz}^{\pm}}{dt} \\ \frac{d\sigma_{xy}^{\pm}}{dt} \\ \frac{d\sigma_{xz}^{\pm}}{dt} \\ \frac{d\sigma_{yz}^{\pm}}{dt} \end{pmatrix} \end{pmatrix} = \mathbf{D}\mathbf{U}^{\pm} - \left(I_9 \otimes H_q^{-1} \otimes I_r \otimes I_s\right)\mathbf{E}^{\pm}\sqrt{\mathbf{q}_x^2+\mathbf{q}_y^2+\mathbf{q}_z^2}\begin{pmatrix} \alpha_x\mathbf{F}_x^{\pm} \\ \alpha_y\mathbf{F}_y^{\pm} \\ \alpha_z\mathbf{F}_z^{\pm} \\ \mp\theta_x n_x\widetilde{\mathbf{F}}_x^{\pm} \\ \mp\theta_y n_y\widetilde{\mathbf{F}}_y^{\pm} \\ \mp\theta_z n_z\widetilde{\mathbf{F}}_z^{\pm} \\ \mp\left(\theta_x n_y\widetilde{\mathbf{F}}_x^{\pm}+\theta_y n_x\widetilde{\mathbf{F}}_y^{\pm}\right) \\ \mp\left(\theta_x n_z\widetilde{\mathbf{F}}_x^{\pm}+\theta_z n_x\widetilde{\mathbf{F}}_z^{\pm}\right) \\ \mp\left(\theta_y n_z\widetilde{\mathbf{F}}_y^{\pm}+\theta_z n_y\widetilde{\mathbf{F}}_z^{\pm}\right) \end{pmatrix}. \tag{67}$$

Note again that, n_x, n_y, n_z are the components of the unit normal $\mathbf{n}$ pointing into the right block, and the dimensionless real numbers α_x, α_y, α_z and θ_x, θ_y, θ_z are penalty parameters determined by requiring stability. The matrices $\mathbf{E}^- = \left(I_9 \otimes E_{Rq} \otimes I_r \otimes I_s\right)$, $\mathbf{E}^+ = \left(I_9 \otimes E_{Lq} \otimes I_r \otimes I_s\right)$ project the SAT terms on the interface. Since we know the solutions at the initial time we can advance (67) in time using an explicit time-stepping scheme. In the numerical experiments presented below we have used the low storage explicit fourth order accurate Runge–Kutta numerical time integrator [8].

4.6. Discrete stability of the interface treatments

In this subsection, we prove the numerical stability of the interface treatment (67). To begin, we set $\alpha_x = \alpha_y = \alpha_z = 1$, $\theta_x = \theta_y = \theta_z = 1$, and consider the equations corresponding to the superscript $-/+$, separately. For $-$, multiply (67) by $\left(\mathbf{v}_x^-, \mathbf{v}_y^-, \mathbf{v}_z^-, \sigma_{xx}^-, \sigma_{yy}^-, \sigma_{zz}^-, \sigma_{xy}^-, \sigma_{xz}^-, \sigma_{yz}^-\right)\mathbf{H}_{qrs}\mathbf{J}_{qrs}$, from the left, and for $+$ multiply (67) by $\left(\mathbf{v}_x^+, \mathbf{v}_y^+, \mathbf{v}_z^+, \sigma_{xx}^+, \sigma_{yy}^+, \sigma_{zz}^+, \sigma_{xy}^+, \sigma_{xz}^+, \sigma_{yz}^+\right)\mathbf{H}_{qrs}\mathbf{J}_{qrs}$, from the left. Thus, using the SBP property (48) or (49) for the momentum equations only, the interior terms cancel out. By summing the two products and ignoring all boundary terms except the terms on the interface we have

$$\begin{aligned} \frac{d}{dt}\left(\mathbf{E}_{Jh}^- + \mathbf{E}_{Jh}^+\right) = &\sum_{j=1}^{N_r}\sum_{k=1}^{N_s}|\mathbf{q}_{Njk}|\left(-\left(\mathbf{v}^-\right)^T\mathbf{F}^- + \left(\mathbf{v}^-\right)^T\mathbf{T}^- - \left(\mathbf{T}^-\right)^T\widetilde{\mathbf{F}}^-\right)J_{N_q jk}h_{jj}^{(r)}h_{kk}^{(s)} \\ &+\sum_{j=1}^{N_r}\sum_{k=1}^{N_s}|\mathbf{q}_{Njk}|\left(-\left(\mathbf{v}^+\right)^T\mathbf{F}^+ - \left(\mathbf{v}^+\right)^T\mathbf{T}^+ + \left(\mathbf{T}^+\right)^T\widetilde{\mathbf{F}}^+\right)J_{N_q jk}h_{jj}^{(r)}h_{kk}^{(s)}. \end{aligned} \tag{68}$$

Defining

$$q_j^{\pm} = Z_j^{\pm}v_j^{\pm} + T_j^{\pm}, \quad p_j^{\pm} = Z_j^{\pm}v_j^{\pm} - T_j^{\pm}, \quad \widehat{q}_j^- = Z_j^-\widehat{v}_j^- + \widehat{T}_j, \quad \widehat{p}_j^+ = Z_j^+\widehat{v}_j^+ - \widehat{T}_j, \quad j = l,m,n,$$

then we have

$$-\left(\mathbf{v}^-\right)^T\mathbf{F}^- + \left(\mathbf{v}^-\right)^T\mathbf{T}^- - \left(\mathbf{T}^-\right)^T\widetilde{\mathbf{F}}^- = -\sum_{j=l,m,n}\frac{1}{4Z_j^-}\left(\left(q_j^- - \widehat{q}_j^-\right)^2 + \left(p_j^-\right)^2 - \left(\widehat{q}_j^-\right)^2\right), \tag{69}$$

$$-\left(\mathbf{v}^+\right)^T\mathbf{F}^+ - \left(\mathbf{v}^+\right)^T\mathbf{T}^+ + \left(\mathbf{T}^+\right)^T\widetilde{\mathbf{F}}^+ = -\sum_{j=l,m,n}\frac{1}{4Z_j^+}\left(\left(p_j^+ - \widehat{p}_j^+\right)^2 + \left(q_j^+\right)^2 - \left(\widehat{p}_j^+\right)^2\right). \tag{70}$$

We begin with the following lemma

Lemma 1. *Let $v_j^{\pm}, T_j^{\pm}$ $(j = l,m,n)$ denote the grid-functions for the particle velocities and tractions on the fault, and $\widehat{v}_j^{\pm}, \widehat{T}_j$ $(j = l,m,n)$ denote the corresponding hat-functions satisfying the interface condition (39) exactly. The following statements are true*

$$i.\quad \widehat{q}_j^+ = q_j^+, \quad \widehat{p}_j^- = p_j^-, \tag{71a}$$

$$ii.\quad \left(q_j^+\right)^2 - \left(\widehat{p}_j^+\right)^2 = 4Z_j^+\widehat{v}_j^+\widehat{T}_j, \quad \left(p_j^-\right)^2 - \left(\widehat{q}_j^-\right)^2 = -4Z_j^-\widehat{v}_j^-\widehat{T}_j, \tag{71b}$$

$$iii.\quad [\![\widehat{v}_l]\!]\widehat{T}_l + [\![\widehat{v}_m]\!]\widehat{T}_m + [\![\widehat{v}_n]\!]\widehat{T}_n = \widehat{\sigma}_n f\left(\widehat{V},\psi\right)\widehat{V} \geq 0, \quad \widehat{V} = \sqrt{[\![\widehat{v}_l]\!]^2 + [\![\widehat{v}_m]\!]^2}. \tag{71c}$$

Proof.
i) Equation (71a) is equivalent to (38).
ii) By *i*) above we have

$$\left(p_j^-\right)^2-\left(\widehat{q}_j\right)^2=\left(\widehat{p}_j^-\right)^2-\left(\widehat{q}_j\right)^2=\left(\widehat{p}_j^--\widehat{q}_j^-\right)\left(\widehat{p}_j^-+\widehat{q}_j^-\right)=-4Z_j^-\widehat{v}_j^-\widehat{T}_j,$$
$$\left(q_j^+\right)^2-\left(\widehat{p}_j^+\right)^2=\left(\widehat{q}_j^+\right)^2-\left(\widehat{p}_j^+\right)^2=\left(\widehat{q}_j^+-\widehat{p}_j^+\right)\left(\widehat{q}_j^++\widehat{p}_j^+\right)=4Z_j^+\widehat{v}_j^+\widehat{T}_j.$$

iii) By using (39b)–(39c) and the facts that $\widehat{\sigma}_n\geq 0$ and $f\left(\widehat{V},\psi\right)\widehat{V}\geq 0$, the inequality (71c) holds.

The proof of the lemma is complete. □

By using the expressions (69), (70) and Lemma 1 above, on the right hand side of (68) we have

Theorem 6. *Consider the semi-discrete approximation (67) of the elastic wave equation subject to the interface conditions (32) with a nonlinear friction law and the SAT terms defined in (66). If $\alpha_x=\alpha_y=\alpha_z=1$, $\theta_x=\theta_y=\theta_z=1$, then*

$$\frac{d}{dt}\left(\mathbf{E}_{Jh}^-+\mathbf{E}_{Jh}^+\right)=-\sum_{j=1}^{N_r}\sum_{k=1}^{N_s}|\mathbf{q}_{Njk}|\sum_{i=l,m,n}\left(\frac{1}{4Z_i^-}\left(q_i^--\widehat{q}_i^-\right)^2+\frac{1}{4Z_i^+}\left(p_i^+-\widehat{p}_i^+\right)^2\right)J_{N_qjk}h_{jj}^{(r)}h_{kk}^{(s)}$$
$$-\sum_{j=1}^{N_r}\sum_{k=1}^{N_s}|\mathbf{q}_{Njk}|\widehat{\sigma}_n f\left(\widehat{V},\psi\right)\widehat{V}\,J_{N_qjk}h_{jj}^{(r)}h_{kk}^{(s)}. \tag{72}$$

The semi-discrete approximation (67) is asymptotically stable.

Note that the first term in the right hand side of (72) is a numerical dissipation which will vanish in the limit of mesh refinement. The energy rate in the second term in the right hand side of (72) directly matches the energy dissipation rate in the continuous problem.

Furthermore, we consider the linearization of the friction law about $V=0$ such that $T_m=\alpha[\![v_m]\!]$, $T_l=\alpha[\![v_l]\!]$, $0\leq\alpha<\infty$. There are two limiting cases. The first limit is a frictionless fault $\alpha\to 0$ and the second limit is a locked fault $\alpha\to\infty$. Consider a frictionless fault, we have $\alpha=0\implies T_m=T_l=0$. A locked fault yields, $\alpha=\infty\implies[\![v_l]\!]=[\![v_m]\!]=0$. We then have $[\![\widehat{v}_l]\!]\widehat{T}_l+[\![\widehat{v}_m]\!]\widehat{T}_m=\frac{\alpha}{(\eta_l+\alpha)^2}\Phi_l^2+\frac{\alpha}{(\eta_m+\alpha)^2}\Phi_m^2$, implying that the energy dissipation rate is bounded for all $0\leq\alpha\leq\infty$. This shows that the spectral radius of the discrete spatial operator has an upper bound independent of $\alpha\geq 0$.

5. Test problems

In this section, we present numerical experiments demonstrating the potential power of the method to simulate spontaneous dynamic earthquake ruptures in complex geometries. We first verify numerical accuracy of the discrete approximations using the method of manufactured solutions (MMS). We then present a number of 3D numerical simulations of dynamic earthquake ruptures on a planar fault, and on two different fractal fault surfaces demonstrating the complexities of earthquake ruptures on rough faults. No artificial dissipation is used.

Consider two isotropic linear elastic materials in the three space dimensional blocks Ω_-, Ω_+ separated by a fault in the x-direction

$$\Omega_-:=\left\{(x,y,z)|,\quad a_x\leq x\leq\widetilde{x}(y,z),\quad a_y\leq y\leq b_y,\quad a_z\leq z\leq b_z\right\},$$
$$\Omega_+:=\left\{(x,y,z)|,\quad \widetilde{x}(y,z)\leq x\leq b_x,\quad a_y\leq y\leq b_y,\quad a_z\leq z\leq b_z\right\}. \tag{73}$$

Note that the fault surface is described by the function $\widetilde{x}(y,z)$.

5.1. Accuracy evaluation for a non-planar fault using MMS

In the first test we evaluate numerical accuracy using MMS. Here, the computational domain is defined by

$$a_x=-2\ \text{km},\quad b_x=1.5\ \text{km},\quad a_y=0\ \text{km},\quad b_y=2\ \text{km},\quad a_z=0\ \text{km},\quad b_z=2\ \text{km}, \tag{74}$$

where the fault surface is

$$\widetilde{x}(y,z)=0.1\left(\exp\left(-\frac{(y-1)^2+(z-1)^2}{0.025}\right)+\sin\left(\frac{2\pi}{b_y-a_y}y\right)\sin\left(\frac{2\pi}{b_z-a_z}z\right)\right). \tag{75}$$

A plot of the fault profile (75) separating the elastic blocks is shown in Fig. 3(a). We generate a 3D boundary conforming curvilinear mesh, obeying the fault topography for each elastic block $\Omega_\pm$, using standard transfinite interpolation [20].

Each domain $\Omega_\pm$ is discretized using different grid resolutions. We choose initial data, boundary data and forcing functions to match the exact solutions,

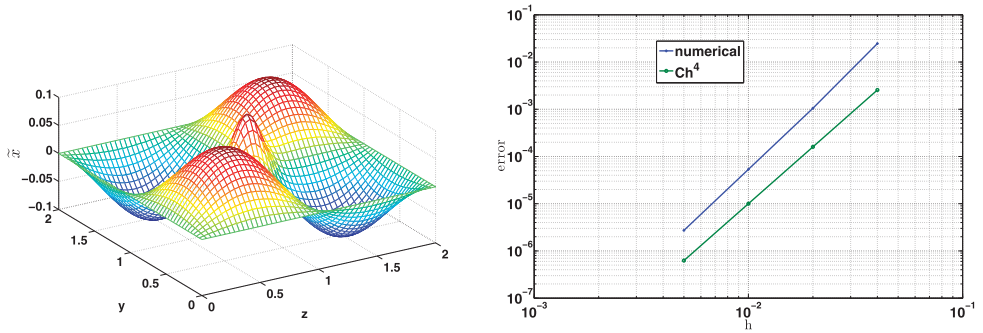

(a) fault profile

(b) L_2-norm of numerical errors using a fourth order accurate Runge–Kutta scheme

Fig. 3. The analytical fault profile used for evaluation of accuracy via MMS and the plot of the error against different spatial resolutions. Note that the convergence rate of the error is fourth order.

$$v_i = \cos(\omega_t \pi t)\sin(k_x \pi x)\sin(k_y \pi y)\sin(k_z \pi z), \quad i = x, y, z,$$
$$\sigma_{ij} = \cos(\omega_t \pi t)\cos(k_x \pi x)\cos(k_y \pi y)\cos(k_z \pi z), \quad i = x, y, z, \quad j = x, y, z, \tag{76}$$

where

$$\omega_t = 2\ \mathrm{s}^{-1}, \quad k_x = k_y = k_z = 1\ \mathrm{km}^{-1}.$$

The material properties in the first block are $\rho = 2600$ kg/m^3, $c_s = 2$ km/s, $c_p = 4$ km/s and the material properties in the second block are $\rho = 2700$ kg/m^3, $c_s = 3.464$ km/s, $c_p = 6$ km/s. Note that the material parameters are discontinuous. Since our aim is to verify accuracy we choose friction parameters such that the numerical solution converges to (76). On the top sides of the blocks, at $y = 2$ km, we impose free-surface boundary conditions. Characteristic boundary conditions are imposed on all other sides of the elastic blocks. We discretize in time using explicit fourth order accurate low-storage Runge–Kutta scheme [8]. The final time is $t = 0.5$ s and the CFL number is 0.5.

The time-step is set using

$$dt = \frac{\mathrm{CFL}}{\max\left(\max_{ijk}\sqrt{q_x^2+q_y^2+q_z^2}c_p, \max_{ijk}\sqrt{r_x^2+r_y^2+r_z^2}c_p, \max_{ijk}\sqrt{s_x^2+s_y^2+s_z^2}c_p\right)}h. \tag{77}$$

Here, $\max c_p = 6$ km/s is the maximum p-wave velocity in the medium. The denominator in (77) corresponds to the maximum eigenvalue of the transformed spatial operator, for the Cauchy problem.

We have run the simulations for different resolutions. Numerical errors, measured in L_2-norm, and the convergence rates are recorded in Fig. 3(b). Note that the errors converge to zero at the expected theoretical accuracy.

5.2. Rupture dynamics on a planar fault

In this experiment we consider a planar fault rupture dynamics benchmark problem 'TPV102' designed by SCEC/USGS Spontaneous Rupture Code Verification Project [25]. Below, we briefly describe the setup and the friction model used in this study.

To begin, we consider a planar strike–slip fault located at $x = 0$ km, bounded in the y- and z-direction by the rectangle, $(y, z) \in [-W, 0] \times [-W, W]$, with $W = 15$ km. The hypocenter is located at the center of the rectangle $(y_0, z_0) = (-7.5\ \mathrm{km}, 0\ \mathrm{km})$ and the boundary at $y = 0$ km is a free-surface. Material properties in the two blocks are homogeneous with $\rho = 2700$ kg/m^3, $c_s = 3.464$ km/s, $c_p = 6$ km/s. The fault is governed by a rate-and-state friction law. The shear strength on the fault evolves according to the nonlinear friction law

$$\tau = a\sigma_n \mathrm{arcsinh}\left(\frac{V}{2V_0}\exp\left(\frac{f_0 + b\ln(V_0\psi/L)}{a}\right)\right), \tag{78}$$

coupled to a state evolution equation defined by the ageing law

$$\frac{d\psi}{dt} = 1 - \frac{V}{L}\psi. \tag{79}$$

The friction parameters V_0, a, f_0, b and L are set Table 1.

To stop the rupture, the friction law changes from velocity-weakening in the rectangular interior region of the fault to velocity-strengthening sufficiently far outside this region. The transition occurs smoothly within a transition layer of width

Table 1
Friction parameters.

f_0	V_0	$a(y,z)$	b	L
0.6	10^{-6} m/s	$0.008 + \Delta a(y,z)$	0.012	0.02 m

Table 2
Initial data.

V_{ini}	τ_{ini}	σ_{ini}
10^{-12} m/s	75 MPa	120 MPa

$w = 3$ km. Outside the transition layer, the fault is made velocity-strengthening by increasing $a(y,z)$ using $\Delta a(y,z) = 0.008\,(1 - \mathrm{B}\,(y - y_0; W/2, w)\,\mathrm{B}\,(z; W, w))$, where

$$\mathrm{B}\,(z; W, w) = \begin{cases} 1, & \text{if} \quad |z| \le W, \\ \frac{1}{2}\left(1 + \tanh\left(\frac{w}{|z|-(W+w)} + \frac{w}{|z|-W}\right)\right), & \text{if} \quad W < |z| < W + w, \\ 0, & \text{if} \quad |z| \ge W + w. \end{cases} \tag{80}$$

The function $\mathrm{B}\,(z; W, w)$ is a smooth version of the boxcar function.

The initial stress tensor is given by

$$\bar{\bar{\sigma}}^0 = \begin{pmatrix} \sigma^0_{xx} & \sigma^0_{xy} & \sigma^0_{xz} \\ \sigma^0_{xy} & \sigma^0_{yy} & \sigma^0_{yz} \\ \sigma^0_{xz} & \sigma^0_{yz} & \sigma^0_{zz} \end{pmatrix}, \tag{81}$$

where

$$\sigma^0_{xx} = -120 \text{ MPa}, \quad \sigma^0_{zz} = -120 \text{ MPa}, \quad \sigma^0_{xz} = 75 \text{ MPa}, \quad \sigma^0_{yy} = \sigma^0_{xy} = \sigma^0_{yz} = 0 \text{ MPa}. \tag{82}$$

We resolve the initial stress on the fault to compute the initial traction vectors

$$\mathbf{T}^0 = \begin{pmatrix} T^0_x \\ T^0_y \\ T^0_z \end{pmatrix} = \bar{\bar{\sigma}}^0 \mathbf{n}, \quad \begin{pmatrix} T^0_n \\ T^0_m \\ T^0_l \end{pmatrix} = \mathbf{R}\mathbf{T}^0. \tag{83}$$

Note that the unit vectors on a planar fault are the canonical basis vectors, thus the normal vector is $\mathbf{n} = (1,0,0)^T$ and the rotation matrix $\mathbf{R}$ is the identity matrix. At $t = 0$, the fault is everywhere sliding in the horizontal direction with initial velocity $V = V_{ini}$. The initial shear stress on the fault, which is also horizontal for the planar fault, is $\tau_{ini} = T^0_l$, the initial normal stress is $\sigma_{ini} = -T^0_n$, and the initial state variable is $\psi_{ini}\,(y,z)$. Note that the initial state variable is spatially variable, but the initial velocity and stresses are uniform. The values of the initial conditions $V_{ini}, \tau_{ini}, \sigma_{ini}$ are given in Table 2.

$$\psi_{ini}\,(y,z) = \frac{L}{V_0} \exp\left(\frac{a\,(y,z) \ln\left(2 \sinh\left(\tau_{ini}/a\,(y,z)\,\sigma_{ini}\right)\right) - f_0 - a\,(y,z) \ln\left(V_{ini}/V_0\right)}{b}\right). \tag{84}$$

Starting at $t = 0$, rupture is nucleated by imposing a horizontal shear traction perturbation, that is

$$T_l = T^0_l + \Delta\tau\,(y,z,t)\,, \tag{85}$$

where

$$\Delta\tau\,(y,z,t) = \Delta\tau_0 F\,(r)\,G(t), \quad r = \sqrt{(y-y_0)^2 + (z-z_0)^2},$$

$$F\,(r) = \begin{cases} \exp\left(\frac{r^2}{r^2-R^2}\right), & \text{if} \quad r < R, \\ 0, & \text{if} \quad r \ge R, \end{cases} \tag{86}$$

$$G\,(t) = \begin{cases} \exp\left(\frac{(t-T)^2}{t(t-2T)}\right), & \text{if} \quad 0 < t < T, \\ 1, & \text{if} \quad t \ge T, \end{cases} \tag{87}$$

with $T = 1$ s, $R = 3$ km, $\Delta\tau_0 = 25$ MPa. The perturbation is smooth in both space and time, it grows from zero to its maximum amplitude $\Delta\tau_0$ over a finite time interval $0 < t \le T$, and is confined to a finite region of the fault of radius R.

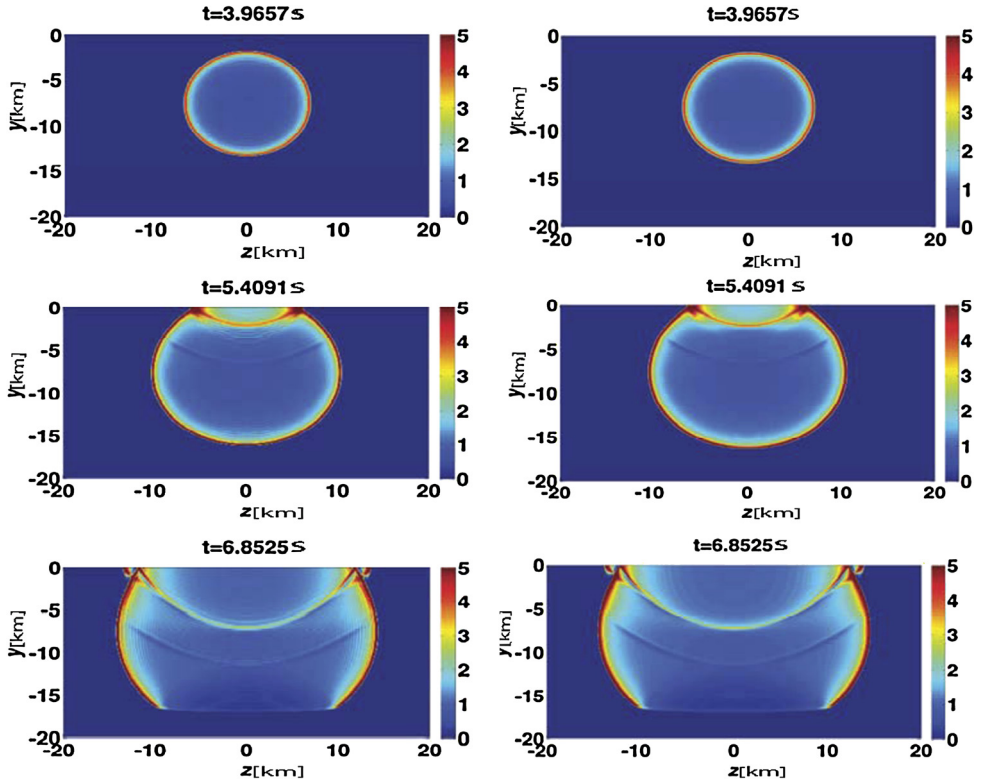

Fig. 4. Snapshots of the slip rates on a planar fault surface using two levels of mesh resolution: with 0.1 km grid spacing for the first column and 0.05 km grid spacing for the second column. Note that the color scale is fixed with the dark red corresponding to the maximum amplitude of the slip velocity which is 5 m/s. (For interpretation of the references to color in this figure legend, the reader is referred to the web version of this article.)

In (73) we set

$$a_x = -20 \text{ km}, \quad b_x = 20 \text{ km}, \quad a_y = 0 \text{ km}, \quad b_y = 20 \text{ km}, \quad a_z = -20 \text{ km}, \quad b_z = 20 \text{ km},$$

and discretize using two levels of grid refinements $201 \times 201 \times 401$ and $401 \times 401 \times 801$ grid points, respectively, for each block, corresponding to 0.1 km and 0.05 km grid spacing in each direction. We run the simulation until the final time $t = 12$ s. Snapshots of the slip rate are shown in Fig. 4. Fig. 5 shows front contours, marking the time at which the fault slip-rate first exceeds 10^{-3} m/s. Rupture starts in the region, centered at the hypocenter $(y_0, z_0) = (-7.5 \text{ km}, 0 \text{ km})$, with the radius $R = 3$ km, and spreads uniformly outward, in all directions. When the rupture reaches the free surface, some of the wave fields are reflected back into the fault but the rupture continues to propagate on the free-surface along the fault. Note also that there are spurious high frequency oscillations trailing the rupture front, see the first column in Fig. 4. This is due to a combination of the large gradients present in the solutions at the rupture tip and the discrete dispersion properties of high order centered finite difference operators for first derivatives on collocated grids. These spurious oscillations can be mitigated by increasing resolution, see the second column in Fig. 4, or the addition of accurately constructed artificial dissipation operators.

In the next subsection, we will present numerical simulations of earthquake rupture dynamics on nonplanar faults, demonstrating the complexity of rupture processes on rough faults.

5.3. Rupture dynamics on nonplanar faults

Here, we consider as before two elastic blocks Ω_-, Ω_+ separated by a fault at $x = \widetilde{x}(y, z)$. The major difference here is that the fault surface is nonplanar. Observations indicate that natural faults are self-similar fractal surfaces with deviations from planarity at all scales [50,7,6]. Recent work [15] in 2D and later by [52] in 3D has shown that dynamic rupture models incorporating geologically constrained fault surface roughness correctly predict near-source ground motion up to $\sim$10 Hz. The extreme stress perturbations associated with slip on nonplanar faults cause fluctuations in rupture velocity and slip. This variability, which destroys the coherence of the high-frequency seismic wavefield, is evidently comparable to that occurring in real earthquakes. We numerically generate a pair (Realization A with minimum wavelength 2 km and Realization B with minimum wavelength 1 km) of random band-limited self-similar faults profiles with roughness quantified in terms of the amplitude-to-wavelength ratio, $\alpha = 10^{-2}$. The fault profiles are shown in Fig. 6. All frictional properties, initial stresses, and material properties are identical to those in the planar fault simulations.

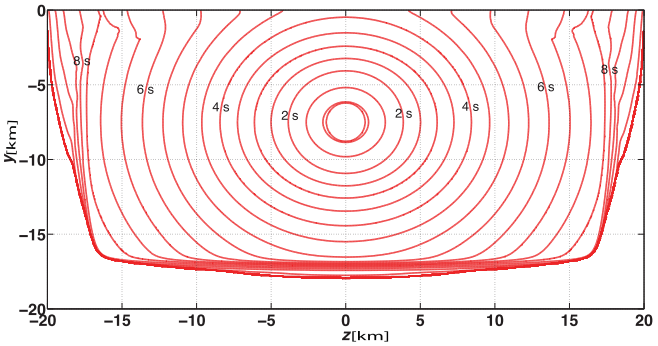

Fig. 5. Rupture contours on a planar fault surface.

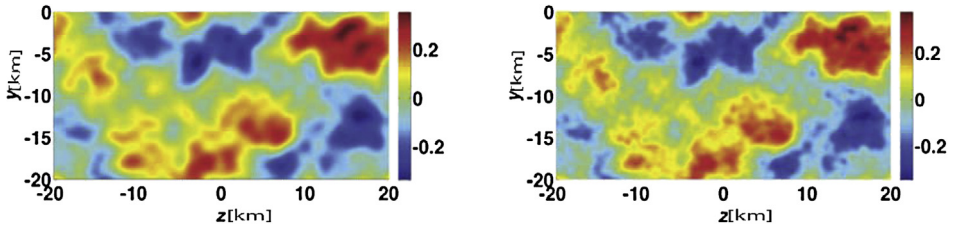

(a) Realization A with minimum wavelength = 2 km (b) Realization B with minimum wavelength = 1 km

Fig. 6. Fractal fault profiles with amplitude-to-wavelength ratio $\alpha = 10^{-2}$.

We generate a 3D curvilinear mesh obeying the fault topography and resolve the stress on the fault to compute the traction vectors. Note that because of the non-planarity of the fault surface the initial tractions on the fault are heterogeneous, even though the initial stress in the medium is homogeneous.

We run the simulations until $t = 12$ s using two levels of grid refinements $201 \times 201 \times 401$ and $401 \times 401 \times 801$ grid points, respectively, for each block. Snapshots of the slip rates for the rough fault profile Fig. 6(a) are shown in the first column of Fig. 7. The rupture contours are shown in Fig. 8. Clearly, fault roughness has a significant effect on the rupture process. As opposed to slip on a planar fault above, slip on nonplanar faults perturbs the stress field in the vicinity of the rupture front, altering its advance and introducing fluctuations in slip and rupture velocity. Those fluctuations, together with changes in the local orientation of the fault, reduce coherence of the seismic wave field. Similar observations were made in [15] for a 2D simulation and in [52] for 3D, respectively. Note that the fault profile in Fig. 6(b) has the same statistical properties as the profile in Fig. 6(a), but now contain shorter wavelength perturbations. The shorter wavelength roughness introduces greater complexity in slip rate and rupture contours, see Fig. 8.

6. Summary and outlook

We have developed a high order accurate and provably stable finite difference method for dynamic earthquake rupture simulations on nonplanar faults embedded in 3D geometrically complex, heterogeneous Earth models. Complex geometries and nonplanar faults are handled using curvilinear grids and coordinate transformation. The transformed equations derived in this paper have much fewer number of terms than the approaches taken in other related studies [40,29,39,32]. This is crucial in minimizing the number of floating points operations, and useful because of the many number of equations and variables describing linear elasticity in 3D. This technique can be extended to other linear hyperbolic problems such as acoustics and Maxwell's equation. We use SBP finite difference operators with sixth order accurate interior stencils and third order accurate boundary closures. However, the method is applicable to all diagonal norm SBP operators. Boundary and interface conditions are imposed weakly using penalties. By deriving penalty parameters and discrete energy estimates, that are analogous to the continuous energy estimates, we prove time stability.

We presented numerical experiments verifying accuracy and demonstrating the usefulness of our method in simulating frictional interface problems in complicated 3D elastic media. We also mention that the code has been benchmarked against problems defined by SCEC/USGS Spontaneous Rupture Code Verification Project. Simulations on self-similar rough fault profiles indicate complex rupture propagation. This software will be used to further understanding of rupture physics and ground motion associated with earthquakes that occur in realistic material structures. Potential applications include problems related to earthquake engineering, induced seismicity, and subduction zone earthquakes.

We also note that our method as well as the continuous Galerkin finite element methods [34,1,14,18] and the spectral element method [27] exhibit spurious high frequency oscillations, trailing the rupture front. This is in part due to large

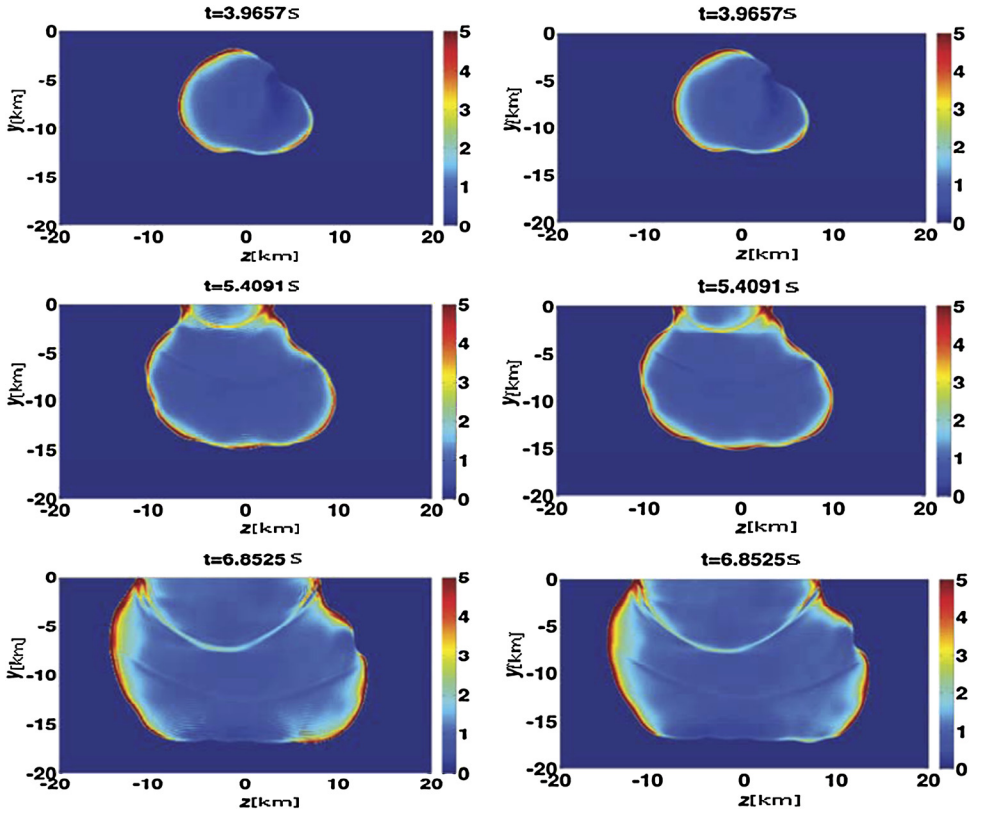

Fig. 7. Snapshots of slip rates on the rough fault profile Realization A, with minimum wavelength = 2 km, using two levels of mesh resolution: with 0.1 km grid spacing for the first column and 0.05 km grid spacing for the second column. Note that the color scale is fixed with the dark red corresponding to the maximum amplitude of the slip rate which is 5 m/s. (For interpretation of the references to color in this figure legend, the reader is referred to the web version of this article.)

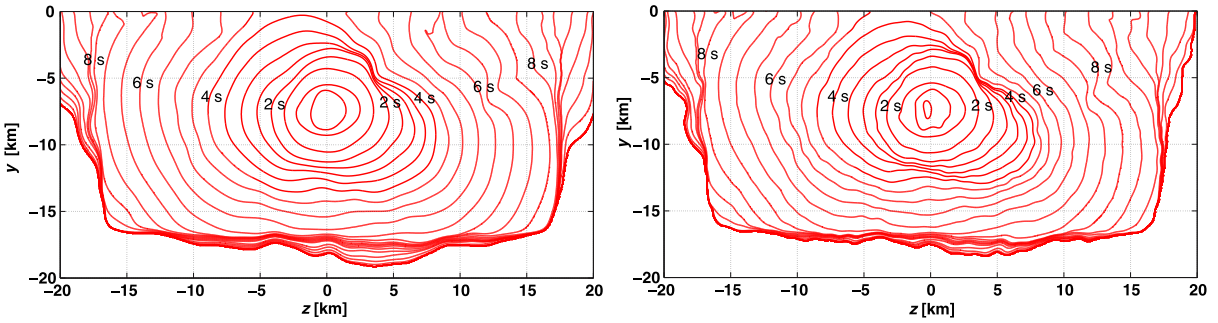

(a) Realization A with minimum wavelength = 2 km (b) Realization B with minimum wavelength = 1 km

Fig. 8. Rupture contours on rough fault surfaces.

gradients present in the solutions at the rupture tip and the non-optimal discrete dispersion properties of the spatial operators. These spurious oscillations can be mitigated by increasing spatial resolution or the addition of accurately constructed artificial dissipation operators. However, artificial dissipation can also introduce some interesting but unfortunately undesirable effects. Probably, a more promising strategy will be to discretize the equation of linear elastodynamics in second order form (where the unknowns are displacements) using minimal stencil second derivative SBP operators [37] for variable coefficients. However, provably stable SBP–SAT methodology for elastic wave equations in second order form and curvilinear grids is rather a recent development [16,17]. Extensions of the SBP–SAT method, for displacement dependent variables, [16,17] to friction laws and rupture dynamics is a topic of future work.

Acknowledgements

This work was supported by the National Science Foundation (ACI-1148493), King Abdullah University of Science and Technology (KAUST) through a joint KAUST Academic Excellence Alliance (AEA) grant with Stanford, and the Southern California Earthquake Center. SCEC is funded by NSF Cooperative Agreement EAR-1033462 and USGS Cooperative Agreement G12AC20038. The SCEC contribution number for this paper is 2062. The numerical simulations were conducted at the Stanford Center for Computational Earth and Environmental Science with computational support by Dennis Michael. The assistance of Samuel Bydlon in making Figs. 1 and 2 is gratefully acknowledged.

References

[1] B.T. Aagaard, Finite-element simulations of earthquakes, PhD thesis, 1999.
[2] D.J. Andrews, Dynamic plane-strain shear rupture with a slip-weakening friction law calculated by a boundary integral method, Bull. Seismol. Soc. Am. 75 (1) (1985) 1–21.
[3] Y. Bar-Sinai, R. Spatschek, E.A. Brener, E. Bouchbinder, Velocity-strengthening friction significantly affects interfacial dynamics, strength and dissipation, Sci. Rep. 5 (7841) (2015), http://dx.doi.org/10.1038/srep07841.
[4] O. Ben-David, G. Cohen, J. Fineberg, The dynamics of the onset of frictional slip, Science 330 (6001) (2010) 211–214.
[5] A. Bizzarri, M. Cocco, D.J. Andrews, E. Boschi, Solving the dynamic rupture problem with different numerical approaches and constitutive laws, Geophys. J. Int. 144 (2001) 656–678.
[6] T. Candela, F. Renard, M. Bouchon, A. Brouste, D. Marsan, J. Schmittbuhl, C. Voisin, Characterization of fault roughness at various scales: implications of three-dimensional high resolution topography measurements, Pure Appl. Geophys. 166 (10) (2009) 1817–1851.
[7] T. Candela, F. Renard, Y. Klinger, K. Mair, J. Schmittbuhl, E.E. Brodsky, Roughness of fault surfaces over nine decades of length scales, J. Geophys. Res. 117 (B8) (2012) B08409, http://dx.doi.org/10.1029/2011JB009041.
[8] M. Carpenter, C. Kennedy, Fourth-order 2N-storage Runge–Kutta schemes, Technical report NASA TM-109112, NASA, Langley Research Center, Hampton, VA, 1994.
[9] M.H. Carpenter, D. Gottlieb, S. Abarbanel, Time-stable boundary conditions for finite-difference schemes solving hyperbolic systems: methodology and application to high-order compact schemes, J. Comput. Phys. 111 (1994) 220–236.
[10] V. Cruz-Atienza, J. Virieux, Dynamic rupture simulation of non-planar faults with a finite-difference approach, Geophys. J. Int. 158 (2004) 939–954.
[11] V. Cruz-Atienza, J. Virieux, H. Aochi, 3D finite-difference dynamic-rupture modeling along nonplanar faults, Geophys. 72 (2007) SM123–SM137.
[12] S. Day, Three-dimensional finite difference simulation of fault dynamics: rectangular faults with fixed rupture velocity, Bull. Seismol. Soc. Am. 72 (1982) 705–727.
[13] J. De La Puente, J. Ampuero, M. Käser, Dynamic rupture modeling on unstructured meshes using a discontinuous Galerkin method, J. Geophys. Res. 114 (2009) B10302.
[14] B. Duan, D. Oglesby, Nonuniform prestress from prior earthquakes and the effect on dynamics of branched fault systems, J. Geophys. Res. 112 (2007) B05308.
[15] E.M. Dunham, D. Belanger, L. Cong, J.E. Kozdon, Earthquake ruptures with strongly rate-weakening friction and off-fault plasticity, 2: nonplanar faults, Bull. Seismol. Soc. Am. 101 (5) (2011) 2308–2322, http://dx.doi.org/10.1785/0120100076.
[16] K. Duru, G. Kreiss, K. Mattsson, Accurate and stable boundary treatments for elastic wave equations in second order formulation, SIAM J. Sci. Comput. 36 (6) (2014) A2787–A2818.
[17] K. Duru, K. Virta, Stable and high order accurate difference methods for the elastic wave equation in discontinuous media, J. Comput. Phys. 279 (2014) 37–62.
[18] G.P. Ely, S.M. Day, J.B. Minster, A support-operator method for viscoelastic wave modelling in 3-D heterogeneous media, Geophys. J. Int. 172 (2008) 331–344.
[19] B.A. Erickson, J. Nordström, Stable, high order accurate adaptive schemes for long time, highly intermittent geophysics problems, J. Comput. Appl. Math. 271 (2014) 328–338.
[20] L.-E. Eriksson, Transfinite mesh generation and computer-aided analysis of mesh effects, Doctoral Dissertation, Department of Computer Science, Uppsala University, Uppsala, Sweden, 1984.
[21] L.B. Freund, The mechanics of dynamic shear crack propagation, J. Geophys. Res. 84 (1979) 2199–2209.
[22] P.H. Geubelle, J.R. Rice, A spectral method for three dimensional elastodynamic fracture problems, J. Mech. Phys. Solids 43 (11) (1995) 1791–1824.
[23] B. Gustafsson, High Order Difference Methods for Time Dependent PDE, Springer-Verlag, Berlin, Heidelberg, 2008.
[24] B. Gustafsson, H.-O. Kreiss, J. Oliger, Time Dependent Problems and Difference Methods, John Wileys and Sons, 1995.
[25] R. Harris, M. Barall, R. Archuleta, E. Dunham, B. Aagaard, J. Ampuero, H. Bhat, V. Cruz-Atienza, L. Dalguer, P. Dawson, S. Day, B. Duan, G. Ely, Y. Kaneko, Y. Kae, N. Lapusta, Y. Liu, S. Ma, D. Oglesby, K. Olsen, A. Pitarka, S. Song, E. Templeton, The SCEC/USGS dynamic earthquake rupture code verification exercise, Seismol. Res. Lett. 80 (2009) 119–126.
[26] A. Johnen, J.-F. Remacle, C. Geuzaine, Geometrical validity of curvilinear finite elements, J. Comput. Phys. 233 (2013) 359–372.
[27] Y. Kaneko, N. Lapusta, J.P. Ampuero, Spectral element modeling of spontaneous earthquake rupture on rate and state faults: effect of velocity-strengthening friction at shallow depths, J. Geophys. Res. 113 (2008) B09317.
[28] D.A. Kopriva, Metric identities and the discontinuous spectral element method on curvilinear meshes, J. Sci. Comput. 26 (2006) 301–327.
[29] D.A. Kopriva, G.J. Gassner, An energy stable discontinuous Galerkin spectral element discretization for variable coefficient advection problems, SIAM J. Sci. Comput. 36 (2014) A2076–A2099.
[30] D.A. Kopriva, G.J. Gassner, Geometry effects in nodal discontinuous Galerkin methods on curved elements that are provably stable, Appl. Math. Comput. (2015) 1–17, http://dx.doi.org/10.1016/j.amc.2015.08.047, available online 8 September 2015.
[31] B.V. Kostov, S. Das, Principles of Earthquake Mechanics, Cambridge University Press, 2005.
[32] J. Kozdon, E. Dunham, J. Nordström, Simulation of dynamic earthquake ruptures in complex geometries using high-order finite difference methods, J. Sci. Comput. 55 (1) (2013) 92–124.
[33] H.-O. Kreiss, J. Lorenz, Initial-Boundary Value Problems and the Navier–Stokes Equations, Academic Press, Boston, USA, 1989.
[34] S. Ma, R.J. Archuleta, P. Liu, Hybrid modeling of elastic p-sv wave motion: a combined finite-element and staggered-grid finite-difference approach, Bull. Seismol. Soc. Am. 94 (2004) 1557–1563.
[35] R. Madariaga, K. Olsen, R. Archuleta, Modeling dynamic rupture in a 3D earthquake fault model, Bull. Seismol. Soc. Am. 88 (1998) 1182–1197.
[36] K. Mattsson, Boundary procedures for summation-by-parts operators, J. Sci. Comput. 18 (2003) 133–153.
[37] K. Mattsson, Summation by parts operators for finite difference approximations of second derivatives with variable coefficients, J. Sci. Comput. 51 (2012) 650–682.

[38] P. Moczo, J. Kristek, M. Galis, P. Pazak, M. Balazovjech, The finite-difference and finite-element modeling of seismic wave propagation and earthquake motion, Acta Phys. Slovaca 57 (2007).
[39] J. Nordström, Conservative finite difference formulations, variable coefficients, energy estimates and artificial dissipation, J. Sci. Comput. 29 (2006) 375–404.
[40] J. Nordström, M.H. Carpenter, High-order finite difference methods, multidimensional linear problems, and curvilinear coordinates, J. Comput. Phys. 173 (1) (2001) 149–174.
[41] A.C. Palmer, J.R. Rice, The growth of slip surfaces in the progressive failure of overconsolidated clay, Proc. R. Soc. Lond. A 332 (1973) 527–548.
[42] C. Pelties, J. de la Puente, J.P. Ampuero, G.B. Brietzke, M. Käser, Three-dimensional dynamic rupture simulation with a high-order discontinuous Galerkin method on unstructured tetrahedral meshes, J. Geophys. Res. 117 (2012) B02309.
[43] T.H. Pulliam, D.W. Zingg, Fundamental Algorithms in Computational Fluid Dynamics, Springer, 2014.
[44] J.R. Rice, The mechanics of earthquake rupture, in physics of the Earth's interior, in: A.M. Dziewonski, E. Boschi (Eds.), Proc. International School of Physics 'Enrico Fermi', Course 78, 1979, Italian Physical Society and North-Holland Publ. Co., 1980, pp. 555–649.
[45] J.R. Rice, Constitutive relations for fault slip and earthquake instabilities, Pure Appl. Geophys. 121 (3) (1983) 443–475.
[46] J.R. Rice, Spatio-temporal complexity of slip on a fault, J. Geophys. Res. 98 (B6) (1993) 9885–9907.
[47] J.R. Rice, A.L. Ruina, Stability of steady frictional slipping, J. Appl. Mech. 50 (2) (1983) 343–349.
[48] J.R. Rice, N. Lapusta, K. Ranjith, Rate and state dependent friction and the stability of sliding between elastically deformable solids, J. Mech. Phys. Solids 49 (9) (2001) 1865–1898.
[49] S.M. Rubinstein, G. Cohen, J. Fineberg, Detachment fronts and the onset of dynamic friction, Nature 430 (2004) 1005–1009.
[50] A. Sagy, E.E. Brodsky, G.J. Axen, Evolution of fault-surface roughness with slip, Geol. 35 (3) (2007) 283–286.
[51] C.H. Scholz, Earthquakes and friction laws, Nature 391 (1998) 37–42.
[52] Z. Shi, S.M. Day, Rupture dynamics and ground motion from 3-D rough-fault simulations, J. Geophys. Res. 118 (3) (2013) 1122–1141.
[53] B. Strand, Summation by parts for finite difference approximations for d/dx, J. Comput. Phys. 110 (1) (1994) 47–67.
[54] M. Svärd, On coordinate transformation for summation-by-parts operators, J. Sci. Comput. 20 (1) (2004) 29–42.
[55] I. Svetlizky, J. Fineberg, Classical shear cracks drive the onset of dry frictional motion, Nature 509 (2014) 205–208.
[56] J. Tago, V. Cruz-Atienza, J. Virieux, V. Etienne, F. Sánchez-Sesma, A 3D hp-adaptive discontinuous Galerkin method for modeling earthquake dynamics, J. Geophys. Res. 117 (2012) B09312.
[57] P.D. Thomas, C.K. Lombard, Geometric conservation law and its application to flow computations on moving grids, AIAA J. 17 (10) (1979) 1030–1037.